ACS APPLIED NANO MATERIALS

The Predictive Synthesis of Monodisperse and Biocompatible Gold Nanoparticles

Alex N. Frickenstein, Nathan Means, Yuxin He, Luke Whitehead, Tekena Harcourt, Zain Malik, Vinit Sheth, Logan Longacre, Haley Taffe, Lin Wang, Isabella McSpadden, Connor Baroody, Wen Yang, Yan D. Zhao, and Stefan Wilhelm*

Cite This: https://doi.org/10.1021/acsanm.4c04838

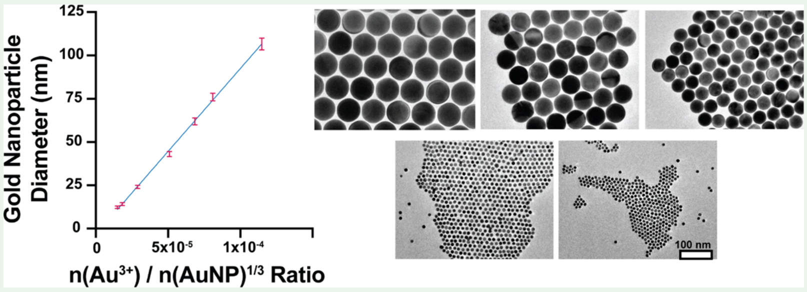

ABSTRACT: The predictive bottom-up synthesis of monodisperse and biocompatible gold nanoparticles using seed-mediated growth procedures is limited by a lack of mathematical models relating reaction components to the final nanoparticle diameter. In this study, we used unique quantitative analytical methods at the single-nanoparticle level to identify the mathematical relationship between the moles of precursor ionic gold and the moles of nanoparticle seeds to synthesize monodisperse gold nanoparticles within ~5% of the target diameter in the ~10 to 120 nm size range. We investigated two commonly used gold nanoparticle syntheses, i.e., the formation of (i) citrate-coated, and (ii) cetyltrimethylammonium chloride (CTAC)-coated gold nanoparticles. Additionally, we developed a surface engineering approach using a physical replacement method that replaces cytotoxic CTAC with biocompatible citrate moieties. We confirmed the successful surface removal of CTAC using several analytical methods and demonstrated biocompatibility with cell viability tests. Our study provides tools and methods by which monodisperse and biocompatible gold nanoparticles can be predictably synthesized for potential downstream biomedical applications.

KEYWORDS: *gold nanoparticles, nanoparticle synthesis, biocompatibility, monodispersity, single particle ICP-MS*

■ INTRODUCTION

Gold nanoparticles (AuNPs) are used extensively as model systems to understand the interactions between nanoparticles and biological systems, such as cells, tissues, and organs.[1−6] Nanomedicine studies using AuNPs have revealed that, among other physicochemical parameters, nanoparticle size, size distribution, shape, and surface chemistry are critical components determining nanoparticle cellular uptake.[7]

One commonly used approach for synthesizing relatively monodisperse and innately biocompatible AuNPs was developed by Perrault and Chan.[8] Here, AuNPs are synthesized using a seed-mediated growth reaction.[8] The resulting AuNPs are coated in citrate and are immediately ready for biomedical applications, given the innate biocompatibility of citrate and relative ease of citrate-coated AuNP surface modification.[9,10] For example, some studies have shown that citrate-coated AuNPs can be used as cancer-disrupting agents.[4,11]

We have previously shown that the before-mentioned citrate-coated AuNPs exhibit a relatively wide size distribution as measured using single-nanoparticle analytical techniques, demonstrating a relative standard deviation (RSD) of ≥10% on average.[12] This broad size distribution can confound the analysis of nanoparticle-cell interactions at the single-particle or single-cell level while complicating the expected fate of nanoparticle doses after *in vivo*administration.[13]

Our recent studies show that AuNPs synthesized using a cetyltrimethylammonium chloride (CTAC)-coated approach exhibit a tighter size distribution (RSD ≤ 10%) compared to citrate-coated AuNPs.[12] Additionally, we have demonstrated

Received: August 22, 2024
Revised: September 11, 2024
Accepted: September 17, 2024

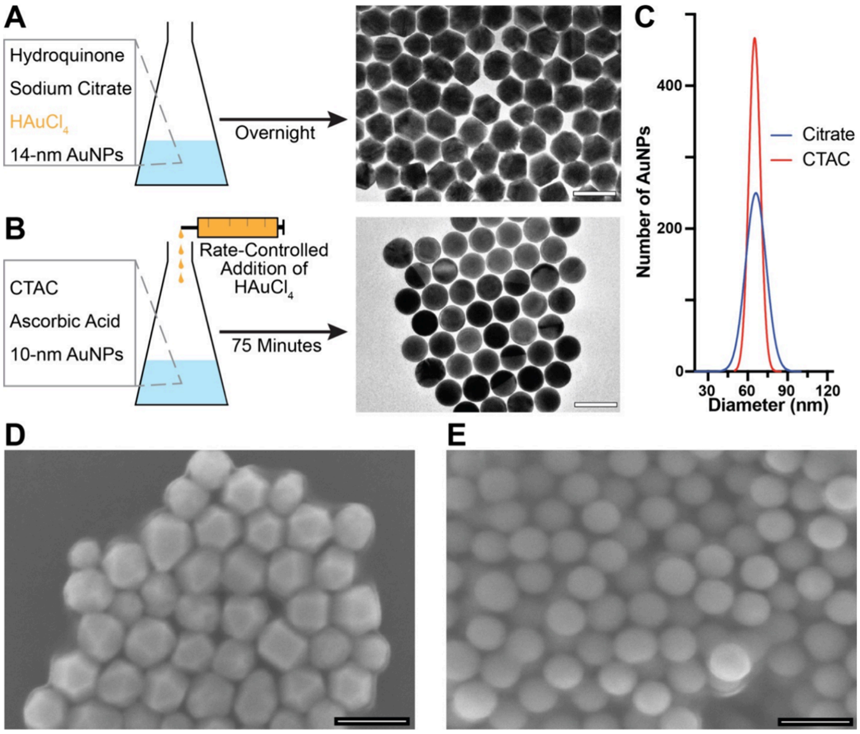

Figure 1. Differences between two seed-mediated nanoparticle reactions and the corresponding nanoparticle outputs. (A) Citrate-coated AuNPs were grown through the simultaneous addition of reaction components—sodium citrate, $HAuCl_4$, hydroquinone (HQ), and 14 nm citrate-coated AuNP seeds—into the reaction vessel. The reaction typically runs overnight before the AuNPs were purified and characterized. The scale bar for the inset TEM image is 100 nm. (B) CTAC-coated AuNPs were grown through controlled dropwise addition of $HAuCl_4$ into a reaction vessel containing CTAC, ascorbic acid, and 10 nm CTAC-coated AuNPs. The reaction was run for 75 min before the AuNPs were purified and characterized. The scale bar for the inset TEM image is 100 nm. (C) Single particle (SP) ICP-MS analysis of diameter distribution from citrate- and CTAC-coated AuNPs. An F test of the data confirms a statistically significant difference in variance ($p < 0.0001$), where variance is an indicator of monodispersity. Data collected for $N = 1000$ AuNPs. See Table S1 for quantification of diameter and monodispersity. (D) Representative SEM image of citrate-coated AuNPs showing the edges and facets of synthesized and purified citrate-coated AuNP surface topology. The scale bar is 100 nm. (E) Representative SEM image of synthesized and purified CTAC-coated AuNPs showing the spherical shape of CTAC-coated AuNP surface topology. The scale bar is 100 nm.

how CTAC-coated AuNPs can be made biocompatible and biofunctional using physical replacement techniques for PEGylation, overcoming the innate cytotoxicity of CTAC.[12,14,15]

However, no mathematical models exist to inform the predictive synthesis of CTAC-coated AuNPs. Such a model would correlate AuNP growth reaction inputs with the final nanoparticle diameter, which is needed to standardize AuNP synthesis and improve confidence in the predicted final synthesis outcomes. Additionally, growing concerns about the immunogenicity of PEG-based nanoparticle surface modifications in clinical settings warrant investigation into alternative CTAC-coated AuNP surface engineering methods.[16,17]

In this study, we addressed these challenges of missing predictive synthesis models and CTAC cytotoxicity. First, we identified and quantified the relationship between the number of AuNP seeds used during the nanoparticle growth reactions and the final AuNP diameter. We quantified the relationship using a mathematical model for two different AuNP growth reactions, i.e., (i) citrate-coated and (ii) CTAC-coated AuNP syntheses, regarding the final AuNP diameter and reaction input ratios. We have previously demonstrated how single-particle inductively coupled plasma mass spectrometry (SP-ICP-MS) can be used to accurately characterize colloidal nanoparticle dispersions in a high-throughput manner with single-particle resolution.[12,18−21]

In the current study, we extensively used SP-ICP-MS to quantify synthesized AuNP size distributions. We affirmed the accuracy of our mathematical models by synthesizing several AuNPs sizes based on model predictions. We also identified a physical replacement method, deemed "citrate physical replacement (citrate-PR)," that removes CTAC from the surface of CTAC-coated AuNPs and replaces it with citrate ions. We demonstrated the successful removal of CTAC by multiple analytical means and showed that AuNP monodispersity is maintained. We further showed a direct comparison between the protein interactions, cell viability, and cell uptake behavior of citrate-coated and post-citrate-PR CTAC-coated AuNPs. Our findings pave the way for accurately predicting AuNP synthesis by citrate- and CTAC-coated methods while providing the baseline for expanded future studies to use highly monodisperse CTAC-coated AuNPs in nanomedicine studies and potential medical applications.

■ RESULTS AND DISCUSSION

Comparison of Gold Nanoparticle Populations Synthesized from Two Different Methods. Our work focused on two different seed-mediated AuNP growth methods. One AuNP growth method uses citrate-coated ~14

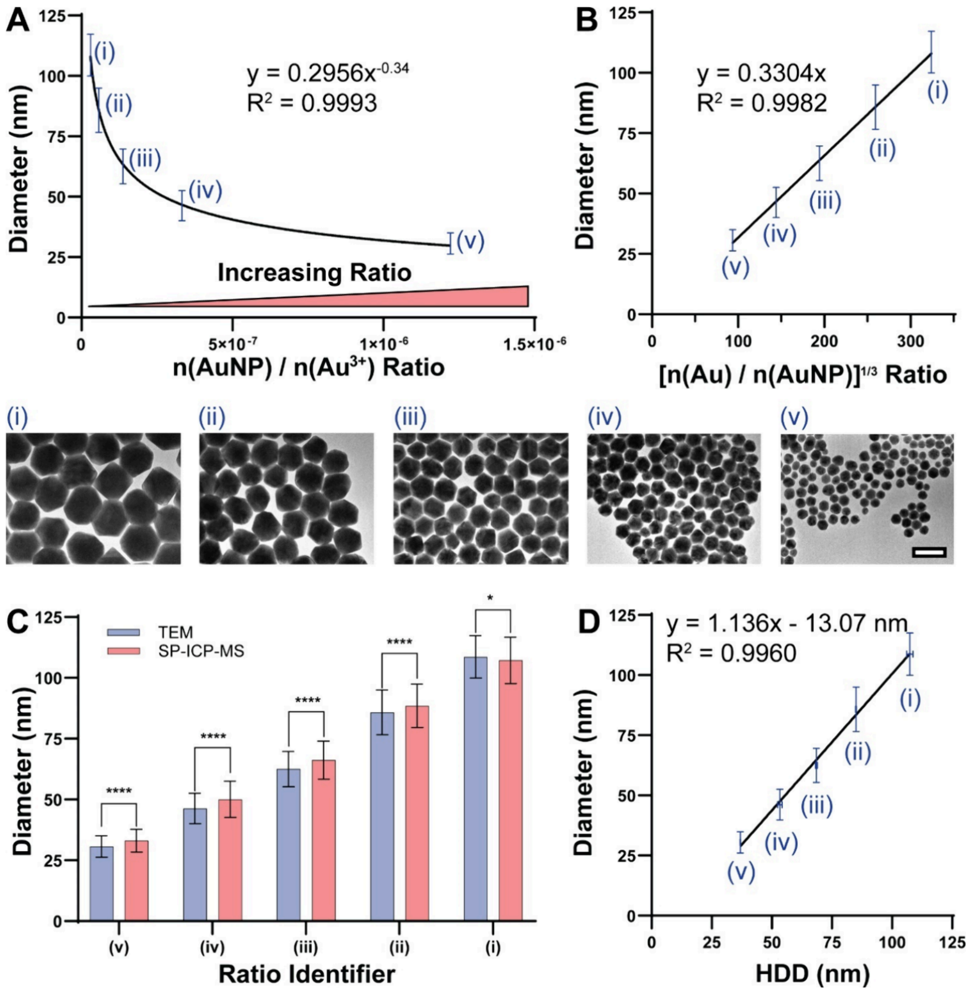

Figure 2. Predictive mathematical modeling of citrate-coated AuNP synthesis. (A) Plot of measured AuNP diameter as determined by TEM and SP-ICP-MS against the ratio of moles of citrate-coated ~14 nm AuNP seeds $n(\text{AuNP})$ used to the moles of precursor Au^{3+} ions used $n(\text{Au}^{3+})$. This ratio is represented in the x-axis as $n(\text{AuNP})/n(\text{Au}^{3+})$, revealing a strong power function correlation ($R^2 > 0.99$). The inset equation shows the power function, where x = the value of the $n(\text{AuNP})/n(\text{Au}^{3+})$ ratio and y = the predicted mean diameter. Inset Roman numerals indicate ratio value identifiers (see Table S2). Mean diameter values were plotted with error bars representing standard deviation. For TEM analysis, $N > 250$ AuNPs were analyzed. For SP-ICP-MS, $N > 750$ AuNPs were analyzed. Inset TEM images (i−v) show AuNPs from all five different $n(\text{AuNP})/n(\text{Au}^{3+})$ ratio numbers and demonstrate an increase in AuNP diameter with decreasing ratio value. The inset image scale bar is 100 nm. (B) Linear form of the relationship between AuNP diameter and modified $n(\text{AuNP})/n(\text{Au}^{3+})$ ratio ($R^2 > 0.99$). Inset Roman numerals indicate ratio value identifiers (see Table S2). (C) Comparison between measured mean diameter values between TEM and SP-ICP-MS. Bar graph shows mean diameter estimates with error bars representing the standard deviation. An unpaired t test analysis on each $n(\text{AuNP})/n(\text{Au}^{3+})$ ratio revealed statistically significant differences in measured mean diameter between TEM and SP-ICP-MS measurements. Despite the apparent statistically significant difference, we assert that TEM and SP-ICP-MS data are comparable given the observed similarity in measured mean diameter values. * = $p < 0.05$, **** = $p < 0.0001$. (D) Plot of measured AuNP diameter as determined by TEM and SP-ICP-MS against the hydrodynamic diameter (HDD) as measured by dynamic light scattering (DLS) reveals a strong linear correlation ($R^2 > 0.99$). Mean values for hydrodynamic diameter and actual diameter are shown with error bars representing standard deviation. Inset Roman numerals indicate ratio value identifiers (see Table S2).

nm AuNP seeds (Figure S1) to produce citrate-coated >14 nm diameter AuNPs using rapid reduction of Au^{3+} precursor ions by hydroquinone (HQ), as shown in Figure 1A.[8,19,22] The second AuNP growth method uses CTAC-coated ~10 nm AuNP seeds (Figure S2) to produce CTAC-coated >10 nm diameter AuNPs using rate-controlled addition of Au^{3+} precursor ions to the reaction, as shown in Figure 1B.[12,23−25]

We have previously detailed differences between citrate- and CTAC-coated AuNPs in terms of population monodispersity and cell viability.[12] In this current study, we show the difference in monodispersity as measured by single-particle inductively coupled mass spectrometry (SP-ICP-MS, Figure 1C).[12,19] The variance (σ^2) of the distribution is an indicator of colloidal monodispersity, whereby a smaller variance indicates a more monodisperse AuNP population. Using an F test, statistical analysis of the AuNP diameter measurements confirms a statistically significant difference in variance ($p < 0.0001$) between citrate-coated AuNPs ($\sigma^2_{\text{citrate}} = 60.8\ \text{nm}^2$) and CTAC-coated AuNPs ($\sigma^2_{\text{CTAC}} = 19.4\ \text{nm}^2$), as reported in Table S1. The statistically significant difference in variance is one indicator that CTAC-coated AuNPs are more monodisperse than citrate-coated AuNPs. Additionally, CTAC-coated AuNPs are more monodisperse compared to citrate-coated AuNPs of the same mean diameter as observed by a ~2× smaller full width at half-maximum (FWHM, eq S1) value and a ~5% decrease in relative standard deviation (RSD, eq S2). Table S1 shows the difference in monodispersity for the AuNPs displayed in Figure 1.

In addition to differing monodispersity, we observed differences in AuNP shape. The TEM images in Figure 1A and Figure 1B show that citrate-coated AuNPs were more polygonal in apparent 2D geometry, whereas CTAC-coated AuNPs were more spherical. We confirmed these observations by scanning electron microscopy (SEM), as shown in Figure 1D for citrate-coated AuNPs and Figure 1E for CTAC-coated AuNPs. The SEM micrographs clearly demonstrate differences in 3D surface topology between the two AuNP populations, where citrate-coated AuNPs show faces, edges, and corners compared to the rounded spherical presentation of CTAC-coated AuNPs. The shape of CTAC AuNPs is largely attributed to the spherical CTAC bilayer around the AuNPs, which controls the AuNP shape during the final etching stages of synthesis.[12,26] By comparison, citrate AuNPs lack shape-controlling features and grow in a rapid and less controlled manner during synthesis, resulting in disparate sizes and shapes of the colloidally dispersed AuNPs.[8] As such, describing citrate-coated AuNPs using measurements of "diameter" is an approximation based on an assumed spherical geometry. This assumption is commonly applied in current literature and is applied in our study.[8,12,19] By these results, we reaffirm that CTAC-coated AuNP synthesis produces more monodisperse particles compared to citrate-coated AuNP synthesis relative to both size distribution as well as shape of individual particles.

Predictive Mathematical Modeling of Synthesized Gold Nanoparticle Diameters. To develop mathematical models correlating molar inputs of reactants with the output AuNP diameter, we first performed seed-mediated AuNP growth for citrate-coated AuNPs using ~14 nm citrate-coated AuNP seeds. Before the growth reaction, we quantified the diameter of the ~14 nm citrate-coated seeds using TEM (Figure S1). We further quantified the concentration of the ~14 nm citrate-coated AuNP seed solution using ultraviolet−visible (UV−vis) spectrophotometry based on Beer−Lambert's Law.[8,12,27,28] Prior studies have shown that the molar extinction coefficient used to estimate nanoparticle concentration heavily depends upon the nanoparticle diameter (eq S3).[8,22,29] As such, small differences in nanoparticle diameter may result in large changes in estimated nanoparticle molar concentration. It is thus critical to obtain an accurate diameter estimate of AuNP seeds used in growth reactions to ensure the accuracy in the molar amount of AuNP seeds being used.

For each growth reaction, we added different molar amounts of ~14 nm AuNP seeds, while keeping all other reactant molar amounts and reaction conditions the same based on established protocols.[8,19,22] Following synthesis, we purified the colloidal dispersions by centrifugation and characterized them using dynamic light scattering (DLS), TEM, and SP-ICP-MS to acquire estimated nanoparticle diameter measurements. We plotted the resulting diameter estimates against the ratio of the moles of AuNPs seeds to the moles of Au^{3+} precursor. We used this ratio, termed the $\frac{n(\mathrm{AuNP})}{n(\mathrm{Au}^{3+})}$ ratio, as a guide for predicting AuNP diameter for different input reaction molar amounts or scaling factors. Our synthesis and quantification results are detailed in Figure 2 and Table S2.

As shown in Figure 2A, our citrate-coated AuNP synthesis results demonstrate a strong correlation between the $\frac{n(\mathrm{AuNP})}{n(\mathrm{Au}^{3+})}$ ratio and the final AuNP diameter as measured by TEM (Figure S3) and SP-ICP-MS (Figures S4, S5 and Table S3). This correlation is defined by eq 1:

$$D_{\mathrm{citrate}} = 0.2956 \times \left(\frac{n(\mathrm{AuNPs})}{n(\mathrm{Au}^{3+})}\right)^{-0.34} \tag{1}$$

where D_{citrate} is the predicted mean diameter of the citrate-coated AuNP population, and $\frac{n(\mathrm{AuNP})}{n(\mathrm{Au}^{3+})}$ is the molar ratio of ~14 nm citrate-coated AuNP seeds to ionic precursor Au^{3+}.

The SP-ICP-MS measurements are reported as the frequency of AuNPs of specific masses. We converted these measurements into estimated diameter frequency values and a correlating AuNP size distribution using eq 2:

$$D_{\mathrm{AuNP}} = \sqrt[3]{\frac{6^{*}m}{\pi^{*}\rho_{\mathrm{Au}}}} \tag{2}$$

where D_{AuNP} is the calculated AuNP diameter, m is the mass of the measured nanoparticle, and ρ_{Au} is the density of gold (19.3 $\frac{\mathrm{g}}{\mathrm{cm}^3}$). The mass data is reported in Table S3.

The mean AuNP diameter was estimated from the Gaussian normal distribution of the measured population, following established methods.[12,18−20] Our plotted results align with previous studies on citrate-coated AuNP growth, which showed a similar trend between the final AuNP diameter and the number of AuNP seeds used in the reaction.[8,30]

By taking the cubic root of the inverse of the $\frac{n(\mathrm{AuNP})}{n(\mathrm{Au}^{3+})}$ ratio, we identify a possible linear correlation between reaction input and final estimated diameter (Figure 2B). We performed this operation based on the cubic relation between the mass of AuNPs and the diameter of AuNPs, assuming a spherical nanoparticle shape, as well as similar reporting methods from other literature.[12,18,19] The result demonstrates the expected linear correlation, indicating our predictive model is reasonable relative to relating nanoparticle geometry (i.e., diameter of a sphere) with reaction inputs (i.e., gold ions).

We compared our TEM mean diameter measurements to our SP-ICP-MS measurements using an unpaired *t* test on each $\frac{n(\mathrm{AuNP})}{n(\mathrm{Au}^{3+})}$ ratio value (Figure 2C). TEM is advantageous for collecting images of synthesized AuNPs, while SP-ICP-MS allows for high-throughput measurement of AuNPs with relatively less sample preparation and data processing.[12,18,19,31] Our statistical analysis reveals a statistically significant ($p < 0.05$) difference between TEM and SP-ICP-MS diameter measurements. We attribute the statistical significance assignment to the large number of AuNPs measured by the single particle analysis methods used. For TEM diameter measurements, $N > 250$ AuNPs were quantified while for SP-ICP-MS diameter measurements, $N > 750$ AuNPs were quantified. We present N values as inequalities since the number of AuNPs that can be quantified per TEM image or per SP-ICP-MS measurement decreases with AuNP size, resulting in lower N values with increasing nanoparticle diameter (i.e., decreasing $\frac{n(\mathrm{AuNP})}{n(\mathrm{Au}^{3+})}$ ratio value). The higher the value of N, the lower the *p*-value will become for a given difference in measured mean values. We assert the differences in measured mean diameter for a given $\frac{n(\mathrm{AuNP})}{n(\mathrm{Au}^{3+})}$ ratio are acceptable based on the magnitude of the differences (<9% change between absolute difference in measured means and measured means themselves for all ratios), as shown in Table S4. Further, we observe from the tabulated data (Table S2), from the plotted SP-ICP-MS and

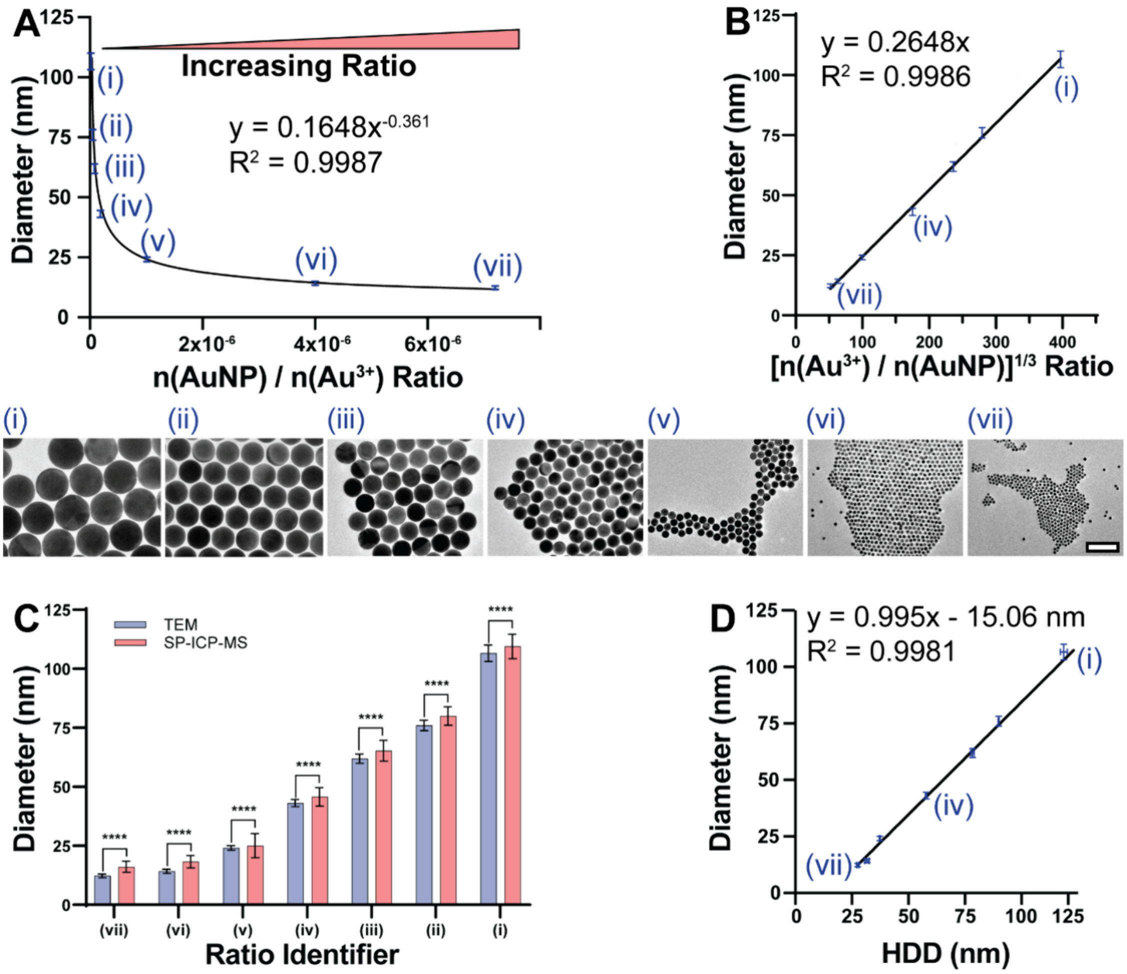

Figure 3. Predictive mathematical modeling of CTAC-coated AuNP synthesis. (A) Plot of measured AuNP diameter as determined by TEM and SP-ICP-MS against the ratio of moles of ∼10 nm CTAC-coated AuNP seeds $n(\mathrm{AuNP})$ used to the moles of Au^{3+} ions $n(\mathrm{Au}^{3+})$ used reveals a strong power function correlation between the two variables. Mean diameter values were plotted with error bars representing standard deviation. For TEM, $N > 250$ AuNPs. For SP-ICP-MS, $N > 750$ AuNPs. Inset TEM images (i−vii) show AuNPs from all different $n(\mathrm{AuNP})/n(\mathrm{Au}^{3+})$ ratio numbers and demonstrate an increase in AuNP diameter with decreasing ratio value. The scale bar is 100 nm. (B) Linear form of the relationship between moles of AuNP seeds and moles of Au^{3+} ions used during the CTAC-coated growth reaction. (C) Comparison between measured mean diameter values between TEM and SP-ICP-MS. Bar graph shows mean diameter estimates with error bars representing the standard deviation. An unpaired t test analysis on each $\mathrm{n(AuNP)/n(Au^{3+})}$ ratio revealed statistically significant differences in measured mean diameter between TEM and SP-ICP-MS measurements. Despite the apparent statistically significant difference, we assert that TEM and SP-ICP-MS data are comparable, given the observed similarity in measured mean diameter values. **** = $p < 0.0001$. (D) Plot of measured AuNP diameter as determined by TEM and SP-ICP-MS against hydrodynamic diameter (HDD) as measured by dynamic light scattering (DLS) reveals a strong linear correlation between the measurements. Mean values for hydrodynamic diameter and actual diameter are shown with error bars representing standard deviation.

TEM diameter data (Figure S6), and from the SP-ICP-MS and TEM diameter distributions with Kolmogorov−Smirnov statistical testing (Figure S7) that TEM and SP-ICP-MS diameter measurements are reasonably similar such that TEM and SP-ICP-MS may be used interchangeably for quantifying AuNP diameter. Additionally, we argue that either TEM or SP-ICP-MS may be used with our predictive synthesis model, acknowledging that SP-ICP-MS is preferred given its more rapid, higher-throughput quantification compared to TEM.

We further quantified the relation between measured hydrodynamic diameter (HDD) by DLS and AuNP diameter (Figure 2D). Based on the sphere of hydration effects, the HDD is expected to be larger than the actual core AuNP diameter.[32,33] This phenomenon is largely observed in our collected data, as shown in Figure 2D and Table S2. For larger synthesized particles (diameter >80 nm), the HDD approaches the same mean diameter estimate as measured by TEM and SP-ICP-MS. We attribute this phenomenon to the scattering of larger particles overcoming the scattering produced by the sphere of hydration.[32] Our results correlating HDD and core diameter provide a guide for estimating AuNP core diameter of citrate-coated AuNPs from DLS data without needing to use complex, expensive instrumentation such as TEM or SP-ICP-MS.

Applying a similar approach to CTAC-coated AuNPs, we varied the mole amount of ∼10 nm CTAC-coated AuNP seeds used in the growth reaction while keeping all other reaction components the same. We characterized the synthesized CTAC-coated AuNPs using DLS, TEM, and SP-ICP-MS and plotted the results using the same approaches applied for our citrate-coated data. We show the results in Figure 3 and Table S5.

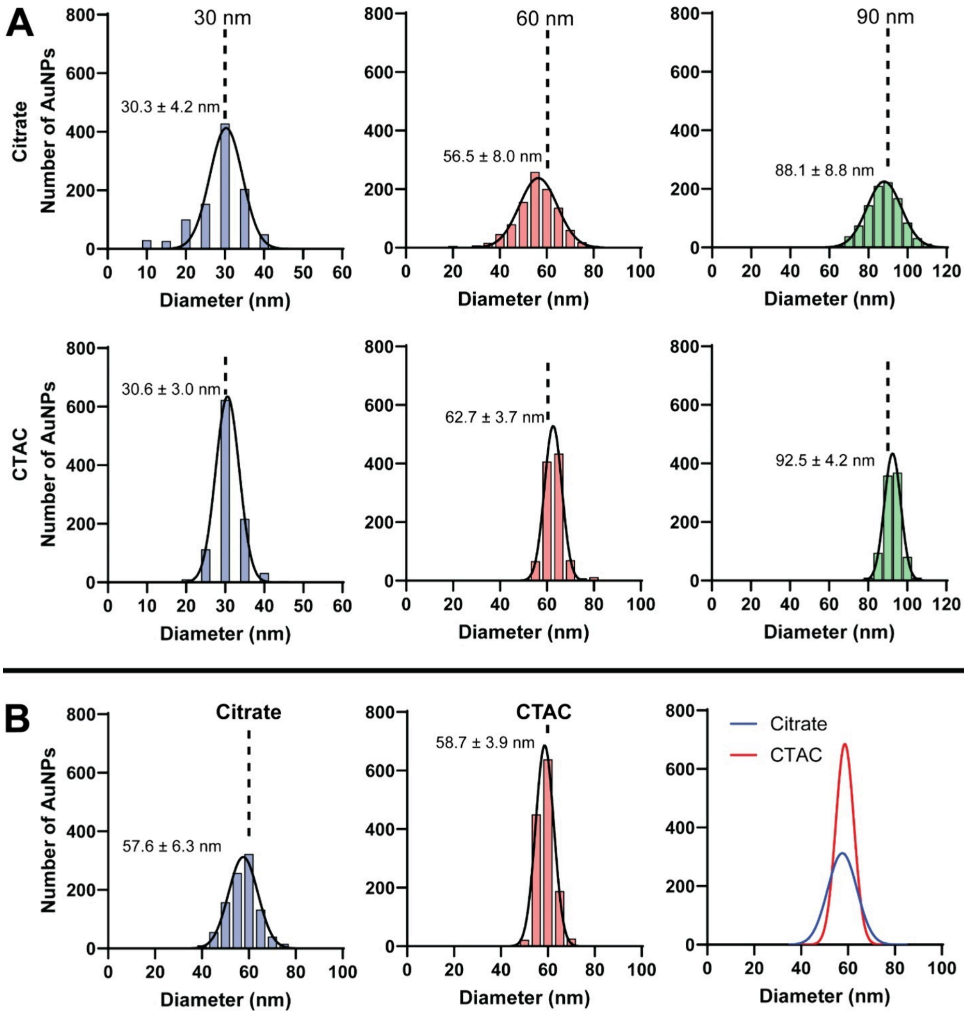

Figure 4. Testing of citrate- and CTAC-coated AuNP predictive growth models using SP-ICP-MS. (A) 30, 60, and 90 nm AuNPs synthesized using citrate-coated and CTAC-coated AuNP approaches were quantified by SP-ICP-MS to test model accuracy. Dashed black lines indicate the desired target nanoparticle diameter. $N = 1000$ AuNPs for each population. Black solid lines represent Gaussian normal fit of the distribution. The resulting mean diameter estimates are within 5% of the target diameter for all synthesized particles. (B) SP-ICP-MS size distribution analysis of 5× reaction scale-up 60 nm citrate-coated AuNPs (blue bars), 5× reaction scale-up 60 nm CTAC-coated AuNPs (red bars), and the overlay of Gaussian normal distribution from SP-ICP-MS measurements. Dashed black lines indicate the desired target nanoparticle diameter. $N = 1000$ AuNPs for each population. Colored lines represent the Gaussian normal fit of the distribution. The resulting mean diameter estimates are within 5% of the target diameter for all synthesized particles.

Our results demonstrate that the relationship between the $\frac{n(\mathrm{AuNP})}{n(\mathrm{Au}^{3+})}$ ratio and the final mean diameter is well-correlated for CTAC-coated AuNPs (Figure 3A) by eq 3:

$$D_{\mathrm{CTAC}} = 0.1648\left(\frac{n(\mathrm{AuNP})}{n(\mathrm{Au}^{3+})}\right)^{-0.361} \tag{3}$$

where D_{CTAC} is the predicted mean diameter of the CTAC-coated AuNPs population, and $\frac{n(\mathrm{AuNP})}{n(\mathrm{Au}^{3+})}$ is the molar ratio of ~10 nm CTAC-coated AuNP seeds to ionic precursor Au^{3+}. We collected AuNP mass data using SP-ICP-MS as shown in Table S6 and calculated diameter estimates using eq 2.

The observed trend is similar to that observed with citrate-coated AuNPs, implying a similar relationship between the molar ratio and the final nanoparticle diameter despite the different synthesis methods. Given that both AuNP types grow by reducing $\mathrm{Au}^{3+}{}_{(aq)}$ to $\mathrm{Au}^{0}{}_{(s)}$ onto the surface of the AuNP seeds or via new nucleation, it is not too surprising to find similar trends in our predictive models.

As with our citrate-coated analysis, we determined a linear correlation between a modified $\frac{n(\mathrm{AuNP})}{n(\mathrm{Au}^{3+})}$ ratio (cubic root of the inverse) and mean diameter by taking the inverse cubic root of the ratio value (Figure 3B). Here again, we see a well-correlated linear trend, affirming our CTAC AuNP predictive model algins well with our understanding of the relation between AuNP geometry (i.e., diameter) and composition (i.e., gold ions). Additionally, we compared the diameter results from TEM (Figure S8) and SP-ICP-MS (eq 2, Figures S9 and S10) to identify any statistically significant difference between measured mean diameters (Figure 3C). As with our citrate-coated results, statistical analysis revealed that there is a statistically significant difference in mean measured diameter between TEM and SP-ICP-MS. Again, we attribute the low calculated p-value to the high N used in our single particle analysis, whereby $N > 250$ for TEM and $N > 750$ for SP-ICP-MS. As from our citrate-coated analysis, we again observe that for most analyzed $\frac{n(\mathrm{AuNP})}{n(\mathrm{Au}^{3+})}$ values, differences between measured mean diameters are acceptable based on the magnitude of the differences. As reported in Table S7, the percent change from the difference in TEM and SP-ICP-MS mean diameter and measured mean diameters themselves is <6% for all ratios except ratio vii and ratio vi. We attribute the larger percent change for ratio vii and ratio vi to the diameter of the AuNPs measured at these $\frac{n(\mathrm{AuNP})}{n(\mathrm{Au}^{3+})}$ ratios. For smaller AuNP diameters, SP-ICP-MS will lose some accuracy due to the instrument's limit of detection.[34] As such, we advise using TEM for smaller AuNPs (≤14 nm) given the improved effective "resolution" compared to SP-ICP-MS. For all other sizes, we recommend SP-ICP-MS given its high-throughput single-particle resolution analysis. Even when considering the outliers of ratio vii and ratio vi (Figure S11A), assessing the linear correlation between TEM and SP-ICP-MS diameter estimates demonstrates support for the similarity between TEM and SP-ICP-MS measurements (Figure S11B). Further, Kolmogorov−Smirnov statistical analysis of the measured diameter distributions reveals no statistically significant differences between TEM and SP-ICP-MS diameter distributions for any $\frac{n(\mathrm{AuNP})}{n(\mathrm{Au}^{3+})}$ ratio value (Figure S12). We still caution against the use of SP-ICP-MS for AuNPs of ≤14 nm diameter, but our data demonstrates that for CTAC-coated AuNPs, TEM and SP-ICP-MS are equally valid in assessing AuNP diameter.

Finally, we plotted the measured HDD from DLS with the measured mean diameter (Figure 3D). We should note that in the case of CTAC-coated AuNPs, the HDD estimate accounts for the CTAC bilayer that is present on the surface of the AuNPs.[12] Thus, the HDD is even further from the actual core diameter estimate compared to citrate-coated AuNPs given the relative size difference between CTAC and citrate molecules. We should further note that for smaller CTAC-coated AuNPs, the linear model shown in Figure 3D becomes less accurate. We attribute this phenomenon to the reduced light scattering efficiency seen from smaller nanoparticles. The CTAC bilayer present on the surface of the AuNPs contributes to the HDD estimate. The smaller the core diameter of the AuNP, the more scattering from the CTAC will influence the net light scattering that occurs during DLS measurements, "masking" the scattering caused by AuNPs. This phenomenon has been shown to affect other smaller nanoparticles as well.[35] As such, for smaller AuNPs (≤14 nm) that are citrate- or CTAC-coated AuNPs, we recommend using TEM imaging over other methods, such as DLS or SP-ICP-MS, for accurate diameter measurements.

Validation of the Predictive Mathematical Models. Having demonstrated the high degree of correlation in our models between the $\frac{n(\mathrm{AuNP})}{n(\mathrm{Au}^{3+})}$ ratio and final AuNP diameter, we sought to test the accuracy of our mathematical models both for targeting specific nanoparticle diameters and maintaining accuracy with reaction scale-up. When discussing scale-up, we refer to 1× scale as using the volumes and concentrations detailed in prior literature and in the Materials and Methods section of this study.[8,12,24] For accurately predicting specific diameters at 1× scale, we synthesized citrate- and CTAC-coated AuNPs with target diameters of 30, 60, and 90 nm to demonstrate the model accuracy across a wide range of target sizes We purified the synthesized colloidal AuNPs by centrifugation and measured the mean diameter using SP-ICP-MS (Figure 4A, Table S8).

Our mathematical models are designed using a molar ratio $\frac{n(\mathrm{AuNP})}{n(\mathrm{Au}^{3+})}$ as the independent variable (x). Per core engineering principles, this allows for easy translation of our models to scale-up of AuNP reactions.[36] The scale-up of AuNP reactions is especially necessary for large in vitro or in vivo experiments that may require a relatively large amount of uniform nanoparticles. Thus, demonstrating the scalability of our proposed reactions is inherently valuable.

To test our model accuracy for scale-up reactions, we performed 5× scale-up synthesis of targeted 60 nm diameter AuNPs for both citrate-coated and CTAC-coated AuNPs. We scaled up the reactions by volume only, keeping the concentration of all reaction components the same as if completing the standard (i.e., 1× scale) synthesis. We purified the 5× scale-up synthesized colloidal AuNPs by centrifugation and characterized them using SP-ICP-MS exclusively (Figure 4B).

We chose to only perform SP-ICP-MS analysis of model and scale testing AuNP populations given the high-throughput nature of SP-ICP-MS and having demonstrated similar mean diameter estimates between TEM and SP-ICP-MS (Figures 2C, S6, 3C, S11).

Based on the mean nanoparticle diameter estimates from our SP-ICP-MS measurement results, we conclude that our models were accurate to within ≤5% of the target diameter. At this level of difference from the target diameter, we argue that there is minimal difference in nanoparticle size-coated behavior. Thus, we are confident our models provide a valuable and accurate guideline for future AuNP synthesis of either citrate-coated or CTAC-coated AuNPs so long as the recommendations and advice discussed are taken into consideration.

We further quantified the yield of the synthesis performed to assess model accuracy. Here, we define yield in terms of the number of nanoparticles of measured estimated diameters that were close to the target diameter of either 30, 60, or 90 nm. We define "on-target" as being within 5% of the target diameter. Our yield results are listed in Table S9.

As seen in Table S9, there is a significant difference in the yield values between citrate-coated and CTAC-coated synthesis approaches. We further show the differences in monodispersity between the citrate-coated and CTAC-coated AuNPs in Table S8. Quantification of yield by particle size is only possible with single-nanoparticle analysis, as we can get an accurate distribution of the diameter of AuNPs in the dispersion. While TEM is a viable method for similar analysis, SP-ICP-MS is better-suited given its high-throughput rapid quantification of nanoparticles.[12,20,31] Thus, we recommend using SP-ICP-MS measurements of AuNP concentration in cases where the exact nanoparticle number needs to be known, though the limit of detection of SP-ICP-MS must be considered relative to the predicted size of the nanoparticles.

Importantly, our results in Table S9 reveal that CTAC-coated AuNP reactions produce more AuNPs that are "on-target" compared to citrate-coated AuNPs. This analysis raises two points worth considering for future nanomedicine research. The first point is to determine what percentage of AuNP dose is responsible for inducing the effect observed. While population-based analysis draws conclusions assuming that 100% of administered AuNPs are of the target size, our analysis reveals that in the case of citrate-coated AuNPs, ≤

40% of administered AuNPs are "on-target" for the desired (i.e., "assumed") diameter. By comparison, 40−70% of CTAC-coated AuNPs are "on-target" for the desired (i.e., "assumed") diameter, revealing a more accurate AuNP population relative to the 100% assumption mentioned earlier.

Based on these differences in yield of "on-target" AuNPs, we conclude that using CTAC-coated AuNPs is a better approach for nanoparticle-size-based nanomedicine experiments that use AuNPs as model nanoparticles. Additionally, our data reveal that there is a need to understand how the different sizes within the size distribution of a given AuNP dose contribute differentially to observed biodistribution and/or efficacy. If this differential effect can be understood, nanoparticles may be better engineered to either (a) design or improve synthesis methods to better approach the assumed 100% "on-target" diameter, or (b) understand how the distribution of sizes may impact nanoparticle fate and subsequent therapeutic effect following dose administration.

Understanding size-based differential effects of administered nanoparticle dose may redefine how nanoparticle dosing is quantified, such as using a dosing approach that is based on the molar concentration of actual on-target nanoparticles with the understanding that <100% of the administered dose is of the desired target size. We leave it to future studies to further investigate these opportunities.

Having confirmed the accuracy of our models, we have developed a tool that users can apply for synthesizing AuNPs of target diameters. Our calculator, provided as a supporting Excel file "Target Diameter Gold Nanoparticle Growth Calculator," can be used to report the necessary solution concentrations and volumes for the synthesis of citrate-coated or CTAC-coated AuNPs of a specific target diameter. Users can also provide a scaling factor for scaling the synthesis up or down based on experiment needs. We provide this tool in the Supporting Information with the goal of bolstering and normalizing AuNP synthesis efforts for future nanoparticle studies.

Considerations for Applying Predictive Models. When applying our models, we encourage considering several aspects of how seed-mediated AuNP growth reactions occur. Our models identify the correlation between final AuNP diameter and the molar ratio of moles of AuNP seeds to moles of gold ions (Au^{3+}) used during synthesis. We have indicated the importance of knowing the diameter of the AuNPs seeds used in the growth reaction given the relationship between AuNP diameter, AuNP molar extinction coefficient, and AuNP concentration estimates.[8,29] We have also shown that for our citrate-coated AuNP model and for our CTAC-coated AuNP model, we used AuNP seeds of ∼14 nm diameter and ∼10 nm diameter, respectively. We selected these seed diameters based upon the literature protocols used for the citrate- and CTAC-coated synthesis reactions.[8,23,24] It is important to note that significant deviations in AuNP seed diameter used in these growth reactions are likely to result in the final AuNP diameter deviating from the diameter predicted by our models.

While we maintain that knowing the AuNP seed diameter is most critical for properly estimating the AuNP seed concentration, we must also recognize that the amount of growth a single AuNP seed can undergo is determined by the AuNP seed diameter itself and the availability of Au^{3+} ions. For example, it is reasonable to conclude that if all other reaction conditions are equivalent, larger AuNP seeds will be expected to have a larger final diameter after the growth reaction finishes compared to smaller AuNP seeds. While the difference between the predicted final AuNP diameter and actual final AuNP diameter is expected to decrease with decreasing $\frac{n(\mathrm{AuNP})}{n(\mathrm{Au}^{3+})}$ ratio, we encourage the use of AuNP seeds that match the sizes used in generating our predictive models. Assessing the relationship between AuNP seed diameter and predicted AuNP diameter with the same $\frac{n(\mathrm{AuNP})}{n(\mathrm{Au}^{3+})}$ ratio may be investigated in the future to increase the robustness and applicability of our current models.

Further, the reaction conditions used to generate our models are worth significant consideration. The pH and temperature of the citrate- and CTAC-coated AuNP seed-mediated growth reactions differ based on the reagents used for the synthesis. pH and temperature play crucial roles in controlling the growth reaction kinetics based on the rate of Au^{3+} reduction and reaction thermodynamics, respectively.[37,38] Deviation in pH or temperature resulting from differing reagents, differing reaction vessel temperature, or differing solvent temperature may all influence the rate at which AuNP growth occurs and, subsequently, alter either the stability of produced AuNPs or the final diameter of produced AuNPs.[37,38]

Our models are based on AuNPs synthesized under specific pH and temperature conditions based on the methods applied. It is important to recognize that seed-mediated growth reactions using alternative reagents or temperature conditions may produce AuNPs that differ from our model predictions. As such, we encourage continuing to use the seed-mediated growth protocols selected for generating our models. Assessing the relationship between our predictive model equation coefficients, temperature, and pH may be investigated in the future to increase the robustness and applicability of our current models.

Understanding the Synthesis Kinetics of CTAC-Coated Gold Nanoparticles. Our predictive mathematical models were computed using nanoparticle diameter estimates of AuNPs taken immediately after purification steps, which were performed immediately after the synthesis was completed. To demonstrate the importance of the timing of purification for CTAC-coated AuNPs, we performed a kinetic analysis of CTAC-coated AuNPs during synthesis using UV−vis spectrophotometry and SP-ICP-MS. We have previously reported on the use of SP-ICP-MS to quantify reaction kinetics for gold−silver alloy nanoparticles at the single-nanoparticle level.[20]

Given the length of time over which CTAC-coated AuNP synthesis occurs, we sought to measure the growth kinetics of CTAC-coated AuNPs using SP-ICP-MS. We focused specifically on CTAC-coated AuNPs as the kinetics of citrate-coated AuNPs have been previously reported.[8] Additionally, the short time scale over which citrate-coated AuNP synthesis occurs due to the rapid reduction action of hydroquinone is not well-suited for characterization by SP-ICP-MS measurements.[8] The kinetics of CTAC-coated AuNP growth have been previously reported using UV−vis spectrophotometry and TEM methods, but SP-ICP-MS analysis has not yet been performed.[39] Further, identifying kinetic trends across different target AuNP diameters has not been explored, indicating an area where our predictive mathematical models can be used to inform size-based growth kinetics of AuNPs.

We collected aliquots from the reaction solution at varying time points throughout the CTAC-coated growth reaction for

30, 60, and 90 nm target diameters of produced AuNPs. Aliquots were characterized by UV−vis spectrophotometry to measure the change in extinction spectra as the reaction progressed (Figure 5A,B). We chose this method of characterization given the color change observed during the reaction. We also measured the change in mean mass with time of 60 nm AuNPs in solution using SP-ICP-MS (Figure 5C).

Our data show that the growth of CTAC-coated AuNPs can be quantified using UV−vis spectrophotometry and SP-ICP-MS characterization. UV−vis spectrophotometry for the growth of 30 nm AuNPs (Figure S13), 60 nm AuNPs (Figure 5A), and 90 nm AuNPs (Figure S14) reveals the same trend in how absorption spectrum changes with time. Until t = 40 min, there is an evident growth of AuNP diameter as observed by the increase in absorption spectrum amplitude and width. After t = 40 min, there is an evident decrease in AuNP diameter as observed by the decrease in absorption spectrum amplitude and width. The trends we observed in our data match prior studies that monitor CTAC-coated AuNP growth by UV−vis spectrophotometry.[39]

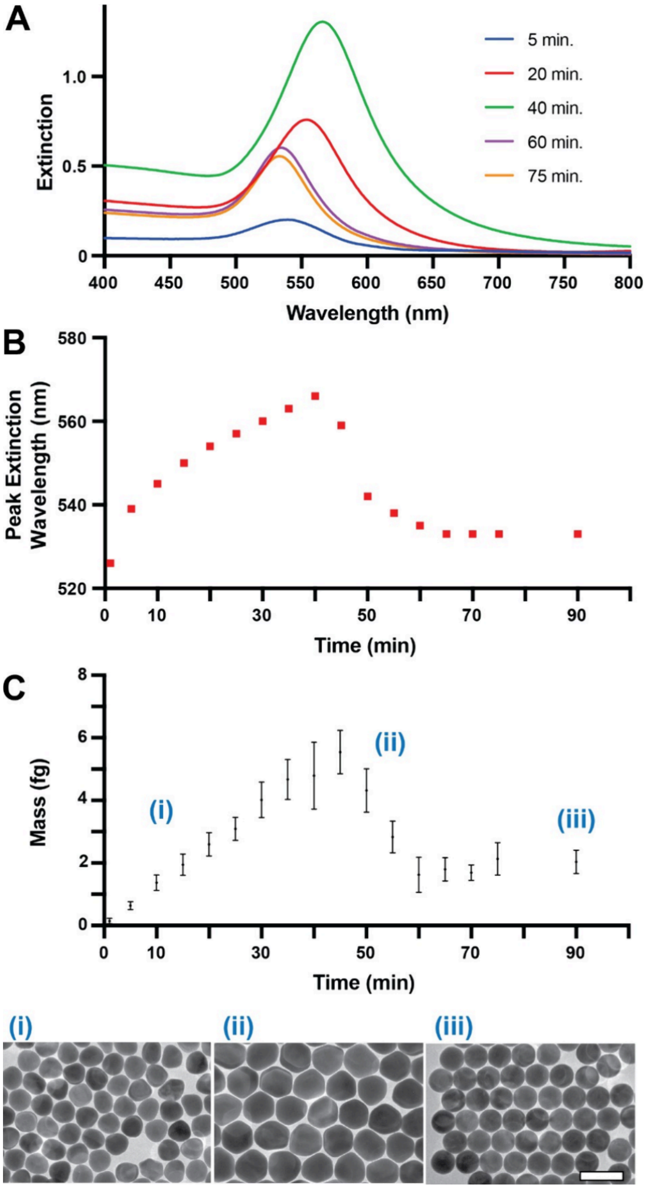

Figure 5. CTAC-coated gold nanoparticle growth kinetics measurements. (A) Change in UV−vis extinction spectra with time for 60 nm diameter CTAC-coated AuNPs during growth reaction. (B) Peak extinction wavelength changes with time for 60 nm diameter synthesized CTAC-coated AuNPs. The 90 min data is representative of the peak extinction wavelength after purification by centrifugation. (C) For 60 nm CTAC-coated AuNPs, the mean mass (error bars = standard deviation) measured by SP-ICP-MS changes with time. The 90 min data are representative of the mean mass after purification centrifugation. Inset TEM images are from (i) t = 15 min, (ii) t = 45 min, and (iii) t = 75 min from left to right. The inset scale bar for TEM micrographs is 100 nm.

We observed that the peak extinction wavelength increased, and the spectrum width increased until t = 40 min. Then, we observed the peak extinction wavelength decreased, and the spectrum narrowed. In terms of how the peak extinction wavelength changes with time, the trend is very similar across all three sizes, the primary difference being the magnitude of the overall change in wavelength with time. The difference in magnitude is expected given that larger AuNPs possess larger extinction wavelengths. Interestingly, the trends observed for both peak extinction wavelength and mean particle mass are very similar in behavior, showing an increase in value up to t = 40 min then a decrease to a final value that stabilizes starting as early as t = 60 min.

Per earlier studies, we attribute the observed trends to the behavior of $AuCl_4^-$ ions in solution during the reaction. It has been identified that CTAC-coated AuNPs undergo a growth phase followed by an etching phase based on the balance between $AuCl_4^-$, CTAC, and ascorbic acid in solution.[39] During the growth phase, AuNP diameter increases, as shown from our data, indicating an increase in UV−vis peak extinction wavelength and an increase in SP-ICP-MS measured mass up to t = 40 min. We collected TEM images that also show this growth over time (Figure 5C). This growth is a result of the reducing action of ascorbic acid on the Au^{3+} ions being added to the reaction in the form of $HAuCl_4$. After ∼40 min, the action of ascorbic acid is diminished in solution and $AuCl_4^-$ interacts with CTAC to form an Au-etching compound that acts on AuNPs in solution.[39] The etching of AuNPs results in the loss of Au content from their structures. We observe this in our results based on the decreased UV−vis spectrophotometry peak extinction wavelength and SP-ICP-MS measured mass after t = 40 min.

Interestingly, we observed a notable change in particle morphology throughout the growth-etching process, whereby the spherical geometry associated with CTAC-coated AuNPs (Figure 1E) is not present until after etching is complete. Initially, growth appears to be less shape-controlled, resulting in a wide variety of shapes and sizes. This phenomenon is likely a contributing factor to the wide UV−vis extinction spectra as well as the SP-ICP-MS mass distributions for all $t \leq 40$ min. After the etching process begins at t = 40 min, the shape appears to become more spherical. Thus, we conclude the shape controlling aspect of CTAC is most efficacious during the etching phase, due to the interaction of $AuCl_4^-$ with CTAC, compared to the growth phase associated with Au^{3+} reduction by ascorbic acid.

From our UV−vis spectrophotometry results, we see an evident difference in the rate of both growth and etching based on the target AuNP diameter, whereby the larger the target diameter, the more rapidly both growth and etching appear to occur. It should be noted that the time at which our reaction switches from growth to etching occurs earlier than in prior

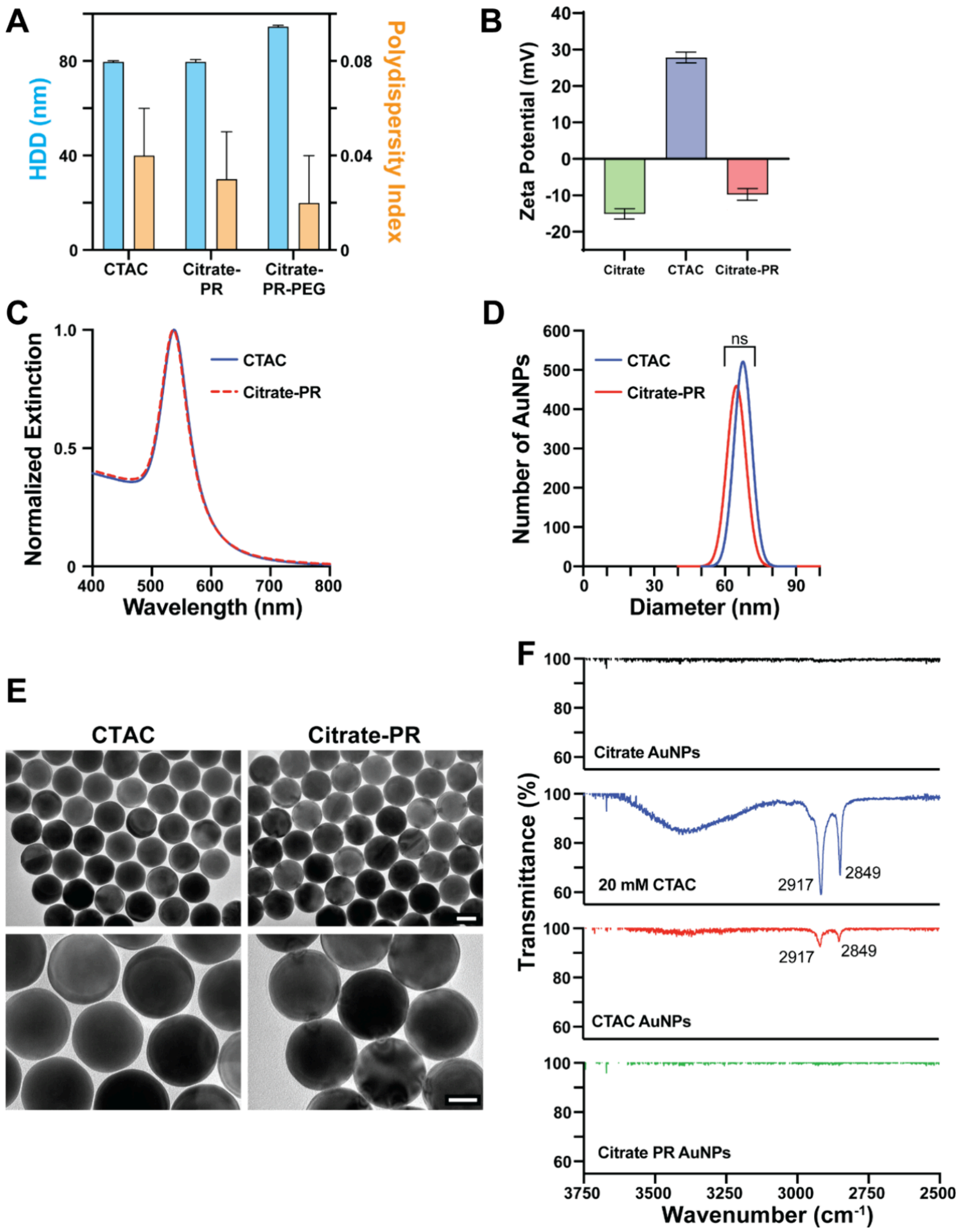

Figure 6. Measuring colloidal stability, monodispersity, and CTAC removal of AuNPs after citrate-PR. (A) Representative HDD and PDI measurements of 60 nm diameter CTAC-coated AuNPs before and after citrate-PR. Blue bars represent mean HDD measurement values, yellow bars represent mean PDI values. Black error bars indicate standard deviation. Data collected for $N = 3$ replicates. (B) Zeta potential measurement mean values of 60 nm diameter citrate-coated AuNPs (green), CTAC-coated AuNPs before citrate-PR (blue), and CTAC-coated AuNPs after citrate-PR (red). Black error bars indicate standard deviation. Data collected for $N = 3$ replicates. (C) UV−vis normalized extinction spectra for 60 nm diameter CTAC-coated AuNPs before and after citrate-PR. (D) SP-ICP-MS normalized Gaussian distribution of AuNP diameter estimates of CTAC-coated AuNPs before and after citrate-PR. $N = 1000$ AuNPs measured. Kolmogorov−Smirnov statistical analysis was run to determine if distributions differ in a statistically significant way. ns = no statistical significance ($p = 0.9864$). (E) Low and high magnification TEM images of 60 nm diameter CTAC-coated AuNPs before and after citrate-PR. Top scale bar (40k × magnification) is 50 nm, bottom scale bar (100k × magnification) is 30 nm. (F) FTIR spectroscopy analysis of 60 nm diameter CTAC-coated AuNPs before and after citrate-PR. Citrate-coated AuNPs and 20-mM CTAC solution were also measured for a negative and positive control, respectively. The transmittance peak values noted in the CTAC AuNPs spectrum are also observed in the 20-mM CTAC spectrum, with the latter having similar transmittance peak values.

studies.[39] We attribute this to differences in reaction conditions, such as reaction temperature. We further emphasize how our findings indicate the importance of purifying CTAC-coated AuNPs immediately after synthesis to avoid continued etching and loss of confidence in predicted AuNP diameter per the predictive models developed in this study.

Surface Modification of CTAC-Coated Gold Nanoparticles. CTAC is innately cytotoxic and must be effectively removed before in vitro or in vivo use. We have previously detailed one method for removing CTAC, i.e., replacing it with poly(ethylene glycol), PEG.[12] While valuable, this approach constrains available surface ligands.

We sought to develop a new method that increases the surface chemistry versatility of originally CTAC-coated AuNPs

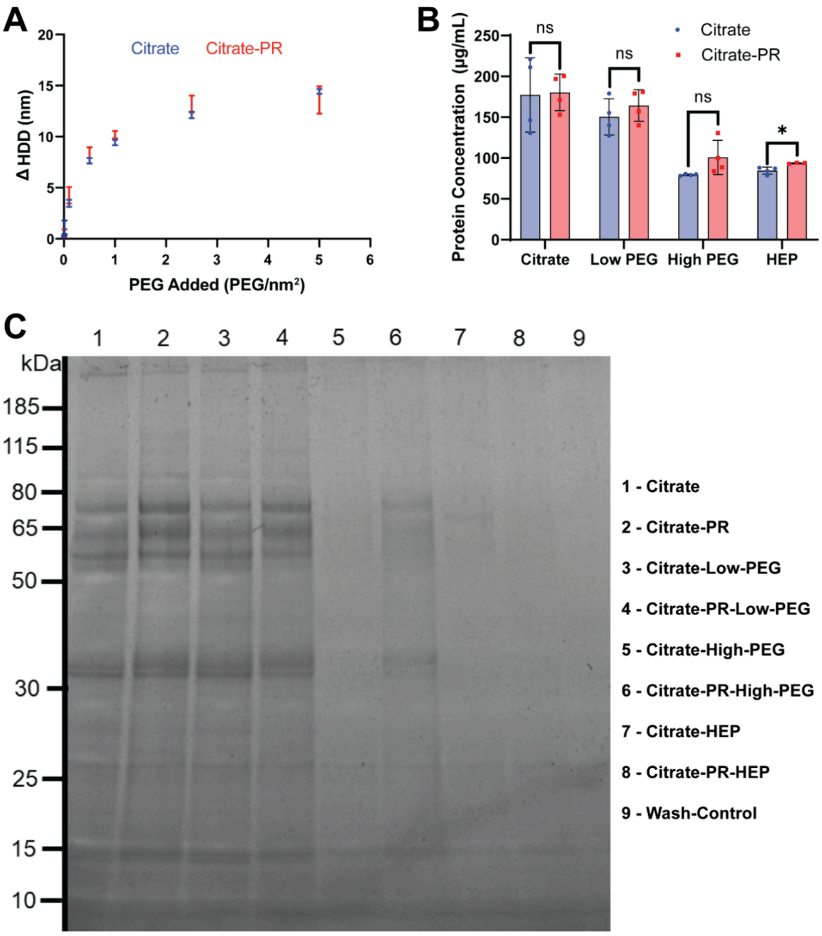

Figure 7. Assessing the surface behavior differences between citrate-coated gold nanoparticles and postcitrate-PR CTAC-coated gold nanoparticles. (A) Change in HDD (ΔHDD) with increasing amount of 5-kDa mPEG-SH added to 60 nm AuNPs. Mean values with error bars are shown. (B) Results of BCA assays demonstrating the relative protein concentration of the analyzed groups. Black error bars represent standard deviation. $N = 4$ replicates were used for each group. One outlier was removed from the citrate-PR HEP group based on Grubbs test analysis of the data ($N = 3$). One-way standard ANOVA was run to assess statistical significance. * = $p < 0.05$, ns = no statistical significance ($p > 0.05$). (C) SDS-PAGE gel revealed protein content of analyzed samples. The legend on the right-hand side clarifies sample identity.

in a size-independent manner. Through the removal of CTAC and subsequent surface conjugation, AuNPs of any diameter can be readily modified. Given CTAC's cytotoxic nature, removal of CTAC is vital to the biomedical applicability of CTAC-coated AuNPs.[14,15] Citrate is a prime choice for a replacement molecule, given its innate biocompatibility and the relative ease with which citrate is removed from the surface of AuNPs when conjugating surface ligands.[8]

We call our process of removing CTAC and replacing it with citrate "citrate-PR" as it uses physical (i.e., mechanical) replacement approaches. The driving force behind our citrate-PR method is the physical removal of CTAC from the surface of CTAC-coated AuNPs in an environment that supports colloidal stability and allows for citrate ions to associate with the surface of the AuNPs. Toward this end, we used sonication and high-speed vortexing (~3200 rcf) to facilitate disruption of the CTAC bilayer around the surface of the CTAC-coated AuNPs in a 1% (v/v) Tween20 solution. Tween20 acts as a surfactant and stabilizing agent to keep AuNPs from aggregating during the citrate-PR process.

Simultaneously, the removal of CTAC by way of sonication, vortexing, and washing by centrifugation allowed for Tween20 and citrate molecules to associate with the AuNP surface. Repeating this process several times increases the confidence in the complete removal of CTAC and the assumed saturation of the AuNP surface with citrate molecules. We characterized AuNPs that underwent citrate-PR using multiple methods, including DLS, zeta-potential measurement, UV−vis spectrophotometry, SP-ICP-MS, TEM, and Fourier transform infrared (FTIR) spectroscopy, as shown in Figure 6.

The polydispersity index (PDI) is a preliminary indicator of changes in colloidal stability that result from nanoparticle aggregation.[19,40] Based on our DLS measurements (Figure 6A), there was no observable difference between the HDD or PDI of our AuNPs before or after citrate-PR. While we may have expected the HDD to decrease slightly as a result of the CTAC bilayer being removed by our citate-PR process, we attribute the maintained HDD value to the presence of the surfactant Tween20, which is known to increase HDD based on measurement mechanics of DLS.[41]

Similar to results from prior studies, our zeta potential data demonstrate a decrease in zeta potential, going from a positive to a negative value (Figures 6B and S15).[12] Given the positive charge associated with CTAC, the decrease in zeta potential value is a strong indicator of CTAC removal from the surface of CTAC-coated AuNPs as a result of our citrate-PR process. We further performed agarose gel electrophoresis to corroborate our zeta potential data (Figure S16, Wells 1−3), wherein CTAC-coated AuNPs aggregated in the well during electrophoresis. In comparison, the citrate-PR AuNPs did not aggregate during electrophoresis and remained colloidally stable. We observed that both the citrate-coated AuNPs and the citrate-PR AuNPs moved toward the anode, further indicating a negative charge is present with citrate-PR AuNPs. The difference in distance traveled likely results from the difference in surface charge between citrate- and citrate-PR AuNPs, as shown in Figure 6B.

The UV−vis spectrophotometry analysis, which can indicate AuNP aggregation and colloidal instability based on increased spectrum width,[19] corroborates the lack of aggregation, projected by DLS PDI measurements, based on the maintained width of the normalized extinction spectrum (Figures 6C and S17). SP-ICP-MS measurements of CTAC-coated AuNPs before and after citrate-PR demonstrated no statistical significance in the AuNP diameter distribution (Figures 6D and S18). Similarly, we detected no observable change in AuNP core shape or size by TEM (Figure 6E). Interestingly, at higher magnification (100k x), we observed that the distance between AuNPs decreased after AuNPs undergo citrate-PR. Likely, this phenomenon is a result of the difference in size between citrate molecule and CTAC. We conclude the CTAC bilayer keeps nearby AuNPs further away compared to the smaller citrate molecules due to steric interactions.

Finally, our FTIR spectroscopy confirmed that CTAC is absent from the surface of CTAC-coated AuNPs after they undergo our citrate-PR method (Figure 6F). The combination of these data suggests that CTAC was successfully removed from the surface of CTAC-coated AuNPs that underwent citrate-PR. By all these metrics, we determined that our citrate-PR process successfully maintained the monodispersity of CTAC-coated AuNPs while removing CTAC. By this, originally CTAC-coated AuNPs may be modified using our citrate-PR method to remove cytotoxic CTAC and replace it with biocompatible citrate while maintaining the narrow size distribution associated with CTAC-coated AuNPs.

Comparing Surface Ligand and Protein Binding Behavior. The development of our citrate-PR method allows for more direct comparison between as-synthesized citrate-coated and postcitrate-PR CTAC-coated AuNPs. After citrate-PR, CTAC-coated AuNPs can be assumed to possess the same surface chemistry as originally synthesized citrate-coated AuNPs. Based on our SEM images (Figure 1D,E), we identified that there are surface topological differences between citrate-coated and CTAC-coated AuNPs. We sought to identify if these topological differences result in any changes in surface ligand density saturation or in interactions between AuNPs and serum proteins. We used previously synthesized 60 nm AuNPs for our analysis, comparing citrate-coated AuNPs to originally CTAC-coated AuNPs that underwent our citrate-PR process. Citrate-coated and citrate-PR AuNPs were modified with PEG or heparosan (HEP) using established methods.[22,42−44]

To determine if the difference in surface topology influenced surface ligand density saturation, we performed PEG saturation analysis similar to prior studies.[22] The PEG used was 5-kDa methoxy-PEG-thiol (mPEG-SH), having a methoxy functional group and a thiol functional group. The thiol functional group allows for formation of Au−S covalent bonds at the surface of the AuNPs, completing PEG conjugation. We plotted our results in terms of the change in HDD with the change in PEG added in terms of the expected number of PEG molecules per nm^2 surface area on the surface of the AuNP (Figure 7A). In addition to quantifying change in HDD by DLS, we also performed agarose gel electrophoresis of AuNPs of each PEG density to identify how PEG density influences electrophoretic behavior (Figure S16, Wells 4−15). Based on the quantitative (DLS) and qualitative (gel electrophoresis) data, we conclude there is not a significant difference between PEG saturation points of citrate-coated and postcitrate-PR CTAC-coated AuNPs despite the observed differences in surface topology (Figure 1). The observed similarity in PEG saturation behavior could be attributed to a couple of factors. First, as we have previously shown, the size distribution of citrate-coated AuNPs is very wide, making direct size-to-size comparison challenging. Second, DLS scattering is influenced more by larger particles in solution. Citrate-coated AuNPs possess AuNPs larger than the target diameter by nature of their large size distribution, as seen by SP-ICP-MS. It is possible that these larger AuNPs shift the HDD estimate higher. An alternative means of quantifying PEG saturation could reveal possible differences between the two AuNP types, though DLS has historically proven an accurate method for such assessment.

Protein analysis of adsorbed serum proteins was assessed using AuNPs of various surface ligands, including citrate, two PEG surface area densities (0.5 and 10 PEG/nm^2), and heparosan (HEP) polysaccharides.[42−44] The surface conjugation of PEG and HEP molecules to AuNPs was verified using DLS quantification of HDD (Table S10). Understanding protein interactions with nanoparticles of different surface properties can inform nanoparticle behavior and fate in vivo.[45]

As with our PEG saturation curves, our results from the bicinchoninic acid (BCA) assay (Figure 7B) and the sodium dodecyl sulfate polyacrylamide gel electrophoresis (SDS-PAGE, Figure 7C) seem to indicate similar protein interaction behavior between the two AuNP populations. In our BCA assay, we observe no statistically significant difference between the two AuNP populations for citrate and PEG surface chemistries ($p > 0.05$) in terms of relative protein amount. This behavior is observed for both low and high PEG densities. Interestingly, our BCA assay revealed a statistically significant difference in relative protein amount between the HEP-conjugated AuNPs ($p = 0.0161$). This difference does not align with what is observed in our SDS-PAGE gel, where we observe no qualitative difference in protein content between HEP-conjugated AuNPs. While the observed difference by BCA assay could be attributed to differences in the surface topology, we do not see similarly significant differences in all other AuNP groups. As such, we recommend future analysis using more refined methods be applied to identify the potential cause of the difference in protein content from the HEP group. As with the PEG analysis, we are using batch-coated methods of analyzing AuNP-protein interactions. Identifying a means of analyzing PEG-AuNP or protein-AuNP interactions at the single particle level may reveal more of a possible difference between the citrate-coated and CTAC-coated AuNPs based on the significant difference in size and shape distributions. Further analysis is recommended to identify the relationships in surface topology and the interactions between AuNPs and surface ligands or serum proteins at the single particle level.

While not used in our BCA or SDS-PAGE analysis, we further conjugated DNA to the surface of postcitrate-PR AuNPs. Our results demonstrate successful DNA conjugation and PEG backfill (Figure S19). With this, the conjugation of postcitrate-PR AuNPs with several different ligands conjugated using different means is shown, indicating the ability of citrate-PR to impart multiple downstream modification opportunities upon originally CTAC-coated AuNPs.

Cell Viability and Uptake. As a final verification of CTAC removal and confirmation of imparted biocompatibility, we performed in vitro analysis of cell viability and AuNP uptake by RAW 264.7 murine macrophages based on established protocols.[12,43,44]

From our cell viability study (Figure 8A), the citrate-PR group possesses a higher cell viability % value than as-synthesized CTAC-coated AuNPs. We conclude that our citrate-PR method imparts biocompatibility to CTAC-coated AuNPs. The data we observed across other surface chemistries are similarly promising, whereby trends in PEG- and HEP-coated AuNPs between citrate- and CTAC-coated AuNPs were similar. Performing the same cell viability experiment with 4T1 mammary tumor mouse cells demonstrated similar trends in cellular viability (Figure S21A).

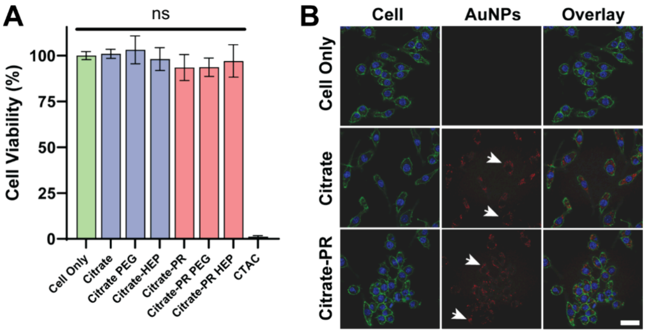

Figure 8. Cell viability and cell uptake analysis of the synthesized gold nanoparticles in macrophages. (A) 2,3-bis(2-methoxy-4-nitro-5-sulphenyl)-(2H)-tetrazolium-5-carboxanilide (XTT) assay cell viability results from treating RAW 264.7 murine macrophages with 0.02-nM of 60 nm AuNPs for 24 h. Green represents cell-only control, blue is for citrate-coated AuNP groups, and red is for CTAC-coated AuNP groups. Values shown are mean cell viability measurements with black error bars representing standard deviation. One-way ANOVA testing was performed to assess statistical significance in data. ns = no statistical significance ($p > 0.05$). $N = 8$ replicates for each group. (B) Confocal Laser Scanning Microscopy (CLSM) images of RAW 264.7 murine macrophages treated with citrate-coated AuNPs or postcitrate-PR CTAC-coated AuNPs. Blue shows the cell nucleus (DAPI), green shows the cell membrane (wheat germ agglutinin-AF488), and red shows scattering of light caused by AuNPs. White arrows point to locations of scattering resulting from AuNP presence. Scale bar is 20 μm.

Confocal laser scanning microscopy (CLSM) imaging (Figures 8B and S20) revealed qualitative nanoparticle uptake by the RAW 264.7 murine macrophages. Nanoparticle-based light scattering revealed the location and relative amount of AuNPs within cells.[46−48] Based on the apparent scattering in both citrate-coated and citrate-PR groups, it appears the AuNP uptake behavior is similar between the two AuNP types. This further demonstrates that our citrate-PR is effective at (a) removing CTAC from the surface of CTAC-coated AuNPs and (b) promotes similar cell uptake behavior to citrate-coated AuNPs. Performing the same uptake experiment with 4T1 mammary tumor mouse cells demonstrated similar trends in cellular uptake for citrate-PR AuNPs compared to citrate-coated AuNPs (Figure S21B). For XTT and CLSM of either the RAW 264.7 murine macrophages or the 4T1 mammary mouse tumor cells, we attribute observed behavior to the AuNPs themselves and to their surface chemistries. We recognize that Tween20, a biocompatible stabilizing agent used during washing and citrate-PR processes, is present during in vitro experiments as AuNPs are concentrated by centrifugation prior to in vitro experiments. The concentration of Tween20 in our treatment doses given to the cells is within reported ranges of nontoxic Tween20 effect (<0.01% v/v).[49] Further, all administered doses except for CTAC-coated AuNPs are expected to have the same concentration of Tween20, indicating that any identified differences result from other factors. Based on these considerations, we are confident that our results accurately reflect the biocompatibility imparted by our citrate-PR process relative to the biocompatibility observed by citrate-coated AuNP synthesis methods.

■ CONCLUSIONS

In this study, we demonstrated how the mean diameter of AuNPs synthesized using citrate-coated or CTAC-coated seed-mediated growth methods can be predicted based on models relating final diameter with $\frac{n(\mathrm{AuNP})}{n(\mathrm{Au}^{3+})}$ ratio values. For both citrate-coated and CTAC-coated AuNPs, our models are accurate to within ∼5% of the target diameter and can be scaled up based on the desired synthesis output. Further, we developed a citrate-PR method by which CTAC can be removed from the surface of originally CTAC-coated AuNPs while maintaining monodispersity. We showed how our citrate-PR method imparts biocompatibility to CTAC-coated AuNPs based on cell-viability and cell uptake experiments. Combined, our results empower several future investigations. First, our predictive synthesis models permit easier AuNP synthesis and are available for public use. The accuracy of our models and the characterization we performed relating TEM, SP-ICP-MS, and HDD data provides synthesis and characterization workflow insight for AuNPs made using citrate-coated or CTAC-coated methods. Additionally, our approach of systematically synthesizing, characterizing, and modeling AuNP growth serves as a benchmark for subsequent nanoparticle characterization studies. In time, our hope is that nanoparticle syntheses may be studied in a similar manner for other nanoparticle formulations. In doing so, we may provide greater confidence and uniformity of nanoparticle synthesis and analysis approaches that normalize preparation methodologies in nanomedicine studies. We also stress the value of citrate-PR in transforming monodisperse CTAC-coated AuNPs into biocompatible and biofunctionalized nanomaterials. We have established the foundation for further investigation into alternative surface modification of citrate-PR CTAC-coated AuNPs and subsequent application in single nanoparticle analysis and nanomedicine studies.

■ MATERIALS AND METHODS

Citrate-Coated AuNP Synthesis. Prior to any synthesis, we cleaned glassware using ∼100 mL of aqua regia comprised of a 3:1 v/v mixture of hydrochloric acid (HCl, SigmaAldrich ACS reagent 37%) and nitric acid (HNO_3, SigmaAldrich ACS reagent 70%). We rinsed aqua regia-treated glassware thoroughly with nanopure water before synthesis. To synthesize citrate-coated AuNPs using the established HQ reduction method, we first made ∼14 nm AuNP seeds based on the well-established Turkevich method.[8,50] We added 1 mL of 30 mg/mL (0.102-M) aqueous sodium citrate tribasic dihydrate (SigmaAldrich S4641) to ∼100 mL of nanopure water inside the cleaned glassware. We mixed the solution gently using a Teflon magnetic stir bar and brought the solution to a boil. We then added 100 μL of a 98.5-mg/mL (0.25-M) solution of $HAuCl_4$ (SigmaAldrich 520918) and stirred the solution vigorously for 7 min. After 7 min, we cooled the solution to room temperature, quenching the reaction, by placing the glassware on an ice bath. Once cooled to room temperature, we characterized the resulting AuNPs by dynamic light scattering (DLS) and ultraviolet spectrophotometry (UV−vis). DLS measurements were collected on a Malvern Zetasizer NanoZS. UV−vis measurements were collected using a UV−vis NIR spectrophotometer (Agilent Cary 5000). AuNPs were stored at 4 °C prior to use. We took a 1 mL aliquot of these AuNP seeds and added 11 μL of a 10% (v/v) Tween20 (SigmaAldrich P9416) solution such that the final Tween20 percentage was 0.01% (v/v). We centrifuged this aliquot at 15,000 relative centrifugal force (rcf, 1× rcf = 1× g-force) for 30 min at 4 °C and removed the supernatant. The resulting pellet was dropped onto a copper TEM grid with copper film (Ted Pella 01813-F) for TEM imaging to determine the exact AuNP seed diameter.

We then synthesized >14 nm AuNPs of different target sizes using established methods.[8,12,22] Across all syntheses performed, we kept the mole amounts of $HAuCl_4$, sodium citrate tribasic dihydrate, and hydroquinone (HQ, SigmaAldrich, H9003) the same and only varied the moles of ∼14 nm AuNP seeds added. In this way, we define the predicted final AuNP diameter resulting from the citrate-coated growth reaction in terms of the ratio of the moles of ∼14 nm AuNP seeds added and of the moles of ionic gold (Au^{3+}) added, henceforth referred to as the $\frac{n(\mathrm{AuNP})}{n(\mathrm{Au}^{3+})}$ ratio. We chose this ratio as our independent variable as it allows for easy reaction scaling based on the target number of AuNPs needed from a given reaction.

We rationally selected $\frac{n(\mathrm{AuNP})}{n(\mathrm{Au}^{3+})}$ ratio values based on prior literature.[8,12,22] We targeted final predicted diameters of less than or equal to 100 nm based on relevance of nanoparticle size in biomedical applications and nanoparticle in vivo behavior.[51−53] Selected ratio values are reported in Table S2. We used established methods as a guide for our syntheses.[8] Prior to synthesis, we measured the approximate concentration of the previously synthesized ∼14 nm AuNP seeds using UV−vis. Once we knew the concentration of the ∼14 nm AuNP seeds, we calculated the milliliter volume of the ∼14 nm AuNP seeds to add to the reaction vessel that would contain 1 mL of 0.025-M $HAuCl_4$ based on the target $\frac{n(\mathrm{AuNP})}{n(\mathrm{Au}^{3+})}$ ratio value (Table S2). Then, to a flask cleaned with aqua regia as previously described, we added chilled nanopure water, 1 mL of 0.025-M $HAuCl_4$, 1 mL of 0.015-M sodium citrate tribasic dihydrate, the calculated mL volume of ∼14 nm AuNP seeds, and 1 mL of 0.025-M HQ under stirring such that the final solution volume in the flask was 100 mL. We let the AuNP growth reaction run overnight prior to characterization by DLS and UV−vis spectrophotometry. To remove excess reactants and smaller AuNPs resulting from new nucleation,[8] we added 1 mL of 10% (v/v) Tween20 to the flask after the reaction was completed. After 10 min, we centrifuged for 90 min at 4 °C. We removed the resulting supernatant and suspended the pellet in ∼10 mL of a 0.1% (v/v) Tween20 0.01% (w/v) sodium citrate tribasic dihydrate solution. We split the solution into 1.5 mL tubes and centrifuged again for 30 min at 4 °C. We removed the supernatant and combined the pellets, diluting to a final volume of ∼1 mL. We adjusted the centrifugation speed based on the estimated AuNP diameter (see Table S2). The purified AuNPs were characterized by DLS, UV−vis spectrophotometry, TEM, and SP-ICP-MS. We collected TEM images using a JEOL-Zeiss 2010F Field Emission TEM with a Direct Electron DE-12 camera. We conducted SP-ICP-MS analysis using a PerkinElmer NexION 2000 with a single cell introduction system (PerkinElmer N8150032) and PerkinElmer Single Cell Application software. A heating element was wrapped around the spray chamber to limit condensation and improve AuNP transport efficiency (TE). We measured TE based on established methods using commercially available 3-μm polystyrene microparticles doped with Lu175 (Fluidigm).[12,18−20] SP-ICP-MS conditions are shown in Table S11.

CTAC-Coated AuNP Synthesis. Prior to any synthesis, any glassware was cleaned using aqua regia, as previously described. The synthesis of CTAC-coated AuNPs occurs in multiple steps according to established protocols.[12,23,24] First, we synthesized precursor Au-clusters that would be used to make the ∼10 nm CTAC AuNP seeds for later reactions. To make Au-clusters, we added 9.5 mL of a 38-M cetyltrimethylammonium bromide (CTAB, Sigma-Aldrich H6269) solution and 500 μL of a 5-mM $HAuCl_4$ solution to a 20 mL cleaned scintillation vial. We heated the vial with the solution to 30 °C and stirred using a Teflon-coated magnetic stir bar for 5 min. We then added 600 μL of a freshly prepared ice-cold 0.1-M sodium borohydride ($NaBH_4$, 213462) solution to the vial under vigorous stirring. After mixing for 2 min, we let the reaction rest at 30 °C for 3 h before measuring the Au-cluster extinction spectrum using UV−vis. Per prior methods, we used the extinction value at a wavelength of 390 nm to estimate the volume of Au-clusters to add for the next step.[12]

Compared to established protocols,[23,24] we scaled-up our synthesis of ∼10 nm CTAC AuNP seeds by 25× to ensure we had enough for subsequent experiments. We first prepared a 110-mM solution of CTAC from a 756-mM CTAC stock solution (SigmaAldrich H292737) and a separate 0.17-M L-ascorbic acid (SigmaAldrich 255564) solution. To a clean 250 mL flask, we added 75 mL of the 110-mM CTAC solution, 10.575 mL of a 0.17-M L-ascorbic acid solution, and 2,246 μL of the previously synthesized Au-clusters. We determined the Au-cluster volume to add based on the extinction value (0.44) at the extinction wavelength of $\lambda = 390$ nm per prior methods.[12] We mixed the resulting solution for 5 min at 25 °C before rapidly adding 25 mL of a 1-mM solution of $HAuCl_4$. We allowed the solution to continue mixing for 15 min before centrifuging for 90 min at 21,000 rcf and 4 °C. We removed the supernatant after centrifugation and resuspended the AuNP pellet in nanopure water. We repeated centrifugation one more time, this time resuspending the AuNP pellet in a 20-mM CTAC solution. The final solution was diluted to a AuNP concentration of ∼5.9 nM as measured by UV−vis spectrophotometry. We characterized the final ∼10 nm CTAC AuNP seeds by DLS, UV−vis, and TEM to estimate colloidal stability and mean diameter. SP-ICP-MS could not be used to characterize CTAC AuNP seeds based on the limits of detection of the method.[34,54]

Using the ∼10 nm CTAC AuNP seeds we synthesized, we proceed to investigate the relationship between the $\frac{n(\mathrm{AuNP})}{n(\mathrm{Au}^{3+})}$ ratio and the final diameter following CTAC-coated growth reaction (see Table S5). We rationally selected $\frac{n(\mathrm{AuNP})}{n(\mathrm{Au}^{3+})}$ ratio values based on prior literature.[12,23,24] To perform CTAC-coated synthesis, we placed a cleaned 250 mL flask onto a hot plate set for 35 °C. Separately, we prepared three solutions. Our first solution (Solution A) was a 100-mM CTAC solution that contained the ∼10 nm CTAC AuNP seeds. The volume of seeds used for each synthesis was determined based on the target $\frac{n(\mathrm{AuNP})}{n(\mathrm{Au}^{3+})}$ compared to the measured concentration of the stock CTAC AuNP seed solution. We set the final volume of Solution A to be 20 mL. We sonicated Solution A for 10 min before adding it to the 250 mL flask to preheat. Our next solution (Solution B) was a 22 mL 0.625-mM $HAuCl_4$ solution. We loaded Solution B into a 30 mL plastic syringe, which was mounted on a Harvard Apparatus PHD ULTRA syringe pump (Harvard Apparatus 703005). The final solution (Solution C) was a 10-mM solution of L-ascorbic acid, which serves as the reducing agent for CTAC-coated growth reactions. We added 1.3 mL of Solution C to the flask containing Solution A and gently mixed for 1 min using a Teflon-coated magnetic stir bar. After 1 min, we started the Harvard syringe pump to begin dropwise addition of Solution B. We set the syringe pump to add solution at a rate of 20 mL/h for 1 h. After 1 h, we allowed the reaction to continue for 15 min before the AuNP solution was immediately centrifuged. As with the citrate-coated synthesis, we varied the centrifugation speeds based on the estimated AuNP diameter (see Table S5). For the first round of centrifugation, we centrifuged for 90 min at 4 °C. We then removed the supernatant, resuspended the AuNP pellet in ∼10 mL of nanopure water, split the solution into 1.5 mL tubes, and centrifuged one more time for 30 min at 4 °C. After this centrifugation, we combined AuNP pellets and resuspended to ∼1 mL using a 20-mM CTAC solution. We characterized the purified AuNPs by DLs, UV−vis, TEM, and SP-ICP-MS.

Characterization of AuNPs and Predictive Model Development. Immediately after synthesis and centrifugation, we characterized AuNPs by dynamic light scattering (DLS) and ultraviolet−visible spectrophotometry (UV−vis) to estimate AuNPs hydrodynamic diameter (HDD), peak absorption wavelength, and concentration in solution. We collected 20−100 μL aliquots of purified and concentrated AuNPs, centrifuged them at a speed appropriate for their estimated diameter (see Tables S2 and S5), and dropped 5-μL of the resulting pellet onto a copper TEM grid with carbon film. We collected TEM images using a JEOL-Zeiss 2010F. We analyzed all collected images using ImageJ to estimate the mean diameter of each synthesized AuNP population.[20] We used the Analyze Particles feature of ImageJ to measure the surface area of each AuNP in each image. We then estimated the diameter of each AuNP, assuming a spherical geometry. We then computed the mean diameter of each AuNP population.

SP-ICP-MS allows for high-throughput analysis of individual nanoparticles in solution with single nanoparticle resolution.[31] We have previously used SP-ICP-MS to characterize AuNP diameter as well as to identify differences in AuNPs based on colloidal stability or synthesis method.[12,19] We used these same methods to identify the mean diameter estimate and relative monodispersity of all synthesized CTAC-coated AuNPs. All SP-ICP-MS measurements of AuNPs were performed on a PerkinElmer NexION 2000 using previously described methods and the conditions described in Table S11.[12,18−20]

We compared mean diameter estimates collected from TEM imaging and from SP-ICP-MS data against each other and against the target $\frac{n(\mathrm{AuNP})}{n(\mathrm{Au}^{3+})}$ ratio values used during AuNP synthesis for both citrate- and CTAC-coated syntheses. We plotted the data and used GraphPad PRISM to identify nonlinear regression results linking the independent variable of the $\frac{n(\mathrm{AuNP})}{n(\mathrm{Au}^{3+})}$ ratio to the dependent variable of the final AuNP diameter. We performed additional analysis using collected data to identify possible correlations between the estimated mean diameter and measured hydrodynamic diameter as determined from DLS measurements. Additionally, we compared mean diameter estimates from TEM and SP-ICP-MS to identify any significant differences between the results from the two single particle analysis methods.

AuNP Predictive Model Testing and Scale-Up. After generating the predictive growth models for both citrate-coated and CTAC-coated AuNP synthesis, we sought to test the apparent accuracy of our models. Using the AuNP growth reactions described, we synthesized citrate-coated and CTAC-coated AuNPs with targeted diameters of 30, 60, and 90 nm. We used our predictive growth models (eqs 1 and 3) to determine the volume of either ∼14 nm citrate AuNP seeds or ∼10 nm CTAC AuNP seeds to use in our respective synthesis approaches. Following synthesis, we purified the AuNPs using centrifugation, as previously described. We quantified the diameter distribution of the resulting synthesized AuNPs using SP-ICP-MS to compare how the final estimated mean diameter compared with the diameter predicted from our models.

As previously described, the final diameter of AuNP growth synthesis reactions can be predicted based on the $\frac{n(\mathrm{AuNP})}{n(\mathrm{Au}^{3+})}$ molar ratio. By defining this relationship in terms of molar ratios, we present an opportunity to easily scale-up AuNP growth synthesis reactions to increase total number of synthesized particles. This approach may prove especially valuable for studies that require large numbers of AuNPs, such as animal studies. To validate that our predictive models remain accurate for scale-up reactions, we synthesized 60 nm target diameter AuNPs using both citrate- and CTAC-coated growth reactions. We scaled-up reactions five times (5×) by volume compared to the normal (i.e., 1×) reaction scale, described previously. Following purification, we quantified AuNP diameter using SP-ICP-MS and compared the mean estimated diameter to the target of 60 nm.

CTAC-Coated AuNP Growth Reaction Kinetics Analysis. Our CTAC-coated AuNP growth reaction occurs over a time span of ∼75 min. During this time, the color of the solution changes, indicating a change in the size of suspended AuNPs. To characterize the growth of AuNPs during the reaction, we synthesized CTAC-coated AuNPs of target diameters 30, 60, and 90 nm using the described synthesis. We used our predictive model (eq 3) to determine the volume of ∼10 nm CTAC seed solution to use for each synthesis. During the reaction, we collected 100 μL of the reaction solution at t = 1 min, 5 min, and every 5 min after until t = 75 min. We used UV−vis spectrophotometry with quartz cuvettes to measure the change in reaction solution extinction spectrum with time. Additionally, for the 60 nm AuNP synthesis, we used SP-ICP-MS to track the changes in mean mass with time and identify AuNP growth kinetics. For SP-ICP-MS measurements, we applied thresholds per prior protocols to remove signal from small AuNPs (i.e., new or original seed nuclei) to better measure the change in AuNP mass with time.[18]

Removal of CTAC from CTAC-Coated AuNPs Using Citrate Physical Replacement (Citrate-PR). To remove CTAC and replace it with biocompatible citrate, we modified our previous method of physical replacement PEGylation.[12] 60 nm diameter CTAC AuNPs were aliquoted into 1.5 mL centrifuge tubes to a volume of 1000-μL and a concentration of 0.2-nM in 0.1% (v/v) Tween20. We centrifuged each tube at 1200 rcf for 30 min at 4 °C. After removing the supernatant, we added 250-μL of a 1% (v/v) Tween20 containing 0.005% (w/v) sodium citrate tribasic dihydrate solution (0.17-mM) to each pellet and sonicated for 10 min. We then vigorously vortexed (∼3200 rcf, Avantor 10153-838) each tube for 2 min before adding 750-μL of 1% (v/v) Tween20 to each tube. This process of centrifugation, sonication, and vortexing was repeated two more times before centrifuging AuNPs one final time. After the final centrifugation, we removed the supernatant, combined pellets from multiple tubes as needed, and resuspended in 0.1% (v/v) Tween20 0.01% (w/v) sodium citrate tribasic dihydrate. We collected approximately 500-μL across multiple tubes at each stage of this process to characterize AuNPs by zeta potential analysis, UV−vis, and SP-ICP-MS to identify changes in surface chemistry resulting from CTAC removal and citrate presence. Prior to using AuNPs for further experiments, AuNPs were then washed two more times by centrifugation using 0.1% (v/v) Tween20 and 0.01% (w/v) sodium citrate tribasic dihydrate solution for resuspension.

There are two principal characteristics we were looking for from AuNPs that had undergone citrate-PR. The first of these was maintained monodispersity expected from CTAC-coated AuNPs. During citrate-PR, we characterized AuNPs by DLS to measure any changes in HDD or PDI. Additionally, we measured the extinction spectrum of AuNPs throughout the citrate-PR process as another way of detecting possible AuNP aggregation. We also collected TEM images of post-PR AuNPs to visually observe any differences in AuNP shape, size, stability, or size distribution. Finally, we performed SP-ICP-MS on AuNPs collected before, during, and after the citrate-PR process to identify any possible changes in colloidal stability or size distribution.

The second principal characteristic we examined was the extent of CTAC removal following citrate-PR. Given that CTAC is positively charged at neutral pH in water, the removal of CTAC from the surface of AuNPs could be detected by collecting zeta potential estimates of AuNPs. We measured the change in zeta potential throughout the citrate-PR process to determine the effective removal of CTAC and replacement with citrate, which is expected to be negatively charged at neutral pH in water. To further verify CTAC replacement with citrate, we performed agarose gel electrophoresis alongside citrate-coated AuNPs of the same target diameter as a positive control. Agarose gel was run using previously established conditions.[43,44] Briefly, we prepared 0.5% (w/v) agarose gel using 0.5× TBE buffer. We added 4-μL of 150-mg/mL Ficoll to 20-μL of concentrated AuNP solutions (0.15-nM). We added the Ficoll-AuNP mixtures to the wells of the agarose gel. We ran gel electrophoresis at 50 V for 90 min before imaging the gel using an Azure C600 imaging system. The AuNP bands were visible without the need for additional imaging instrumentation or methods.

We also performed Fourier transform infrared (FTIR) spectroscopy to identify CTAC removal. CTAC possesses a quaternary amide group that would register as transmission peaks at wavelengths of 2700−3000 cm^{-1} using FTIR.[55−57] We analyzed 60 nm citrate-coated AuNPs, 20-mM CTAC solution, as-synthesized 60 nm CTAC-coated AuNPs, and postcitrate-PR CTAC-coated AuNPs using FTIR to identify any changes in the transmission spectra after our citrate-PR process. FTIR analysis was performed using a Thermo Scientific Nicolet iS-50 with the Attenuated Total Reflection module. We collected a total of 64 scans with a resolution of 1 cm^{-1} for each analyzed sample. We analyzed the collected data using the Omnic Specta software. For each solution, we dropped 20-μL of solution onto the detector of the instrument and let the droplet air-dry for 60−90 min before running the instrument for data collection.

Ligand Conjugation to AuNP Surfaces. After performing citrate-PR, the surface of originally CTAC-coated AuNPs should be capped with citrate molecules and Tween20 surfactant. Based on prior literature, the surface modification of AuNPs with these surface ligands should be readily modifiable with polyethylene glycol (PEG) molecules that possess reactive sulfide groups, such as maleimide.[22] By comparison, CTAC-coated AuNPs are resistant to standard PEGylation methods due to the CTAC bilayer present on the surface of CTAC-coated AuNPs following synthesis.[26] To verify existing potential for surface modification, we PEGylated our post-PR CTAC-coated 60 nm AuNPs using established methods.[22] We prepared a solution of 5-kDa methoxy-terminated thiol PEG, mPEG-SH (Laysan Bio) dissolved in 0.1% (v/v) Tween20 and added post-PR CTAC-coated AuNPs to the solution. We incubated the PEG-AuNP solution for 30 min at room temperature before characterizing. The concentration of the mPEG-SH and the AuNPs was such that the expected molecular surface density of PEG per nanometers squared (PEG/nm^2) of AuNP surface was 10 PEG/nm^2. We selected this target PEG density to ensure the complete saturation of the AuNP surface per prior literature.[22] We then measured the change in HDD using DLS to verify if PEGylation was successful (Table S10).

Based on our collected TEM and SEM images, we identified that there was an apparent difference in the geometry and surface topology between citrate- and CTAC-coated AuNPs. It is well-stablished that surface curvature of AuNPs can influence the binding density of conjugated surface ligands, such as PEG.[22,58] To determine if the topological differences we observed result in changes in ligand binding densities, we synthesized 60 nm citrate- and CTAC-coated AuNPs to identify if the surface ligand saturation point between citrate- and CTAC-coated AuNPs differs. We synthesized citrate- and CTAC-coated AuNPs using the methods described above. We used our diameter predictive models during AuNP synthesis to determine the volume of AuNP seeds to add to achieve the target diameter value of 60 nm. We performed citrate-PR on all CTAC-coated AuNPs using the described method.

We proceeded to PEGylate the 60 nm AuNPs as described, aiming for target ligand density values of 0, 0.01, 0.1, 0.5, 1, 2.5, and 5 PEG molecules per nanometer squared (PEG/nm^2). We selected these target PEG surface densities based on a prior study performing similar analysis.[22] Across each nanoparticle core (citrate-coated or CTAC-coated) and targeted PEG density, samples were prepared in triplicate. We then measured the change in HDD for each sample using DLS. We compared the measured HDD value of PEGylated AuNPs to the HDD value of non-PEGylated AuNPs to quantify the change in HDD for each targeted PEG density. We plotted the resulting change in HDD values against targeted PEG density to identify differences in saturation point between citrate-coated and CTAC-coated AuNPs.

As an alternative surface ligand to PEG, we aimed to assess if heparosan (HEP, Paul DeAngelis Lab) could be successfully conjugated onto the surface of postcitrate-PR CTAC-coated AuNPs.[42−44] HEP was prepared according to prior studies, and we used the pH-salt aging method to perform HEP-conjugation onto the surface of AuNPs.[43,44] We added HCl to nanopure water until the pH was 3.0 as determined by pH probe. We added 13-kDa HEP to the acid water followed immediately by either citrate-coated AuNPs or postcitrate-PR CTAC-coated AuNPs such that the target surface area density of HEP was 10 HEP/nm^2. After incubating at room temperature for 20 min, we added 3.43-M NaCl solution to the HEP-AuNP solution until the concentration of NaCl was 0.3-M and vortexed the solution. After incubating for 20 min at room temperature, we added more 3.43-M NaCl solution until the final concentration of NaCl in the HEP-AuNP solution was 0.6-M. We vortexed the solution and incubated for 20 min at room temperature. We then characterized AuNPs by DLS to verify successful conjugation.

DNA Conjugation to Citrate-PR AuNPs. We synthesized 60 nm CTAC AuNPs and performed citrate-PR as described. Initially, 104-μL of 3.96-nM AuNPs were combined with 40-μL of 0.1% (v/v) Tween and 60-μL of nanopure water in a 1.5 mL Eppendorf tube. Then, 300-μL of 19-μM thiolated DNA (5′-TAACAACGATCCCT-CAAAAAAAAAA—SH-3′, Integrated DNA Technologies) in TE Buffer (10-mM Tris SigmaAldrich 252859, 1-mM EDTA SigmaAldrich EDS) was added to the AuNPs. The DNA sequence was used based on prior literature demonstrating successful conjugation to AuNPs.[59,60] DNA was purified using Illustra NAP-5 columns (GE Healthcare 17-0853-01). After a 30 min incubation, 100-μL of 100-mM sodium citrate tribasic dihydrate at pH 3 was introduced, and the solution was gently vortexed, followed by a 60 min incubation. We then measured HDD and PDI via DLS to confirm DNA conjugation. To stabilize the AuNP-DNA conjugates, we added 50-μL of 2-mM 1-kDa mPEG-SH solution and 700-μL of 0.1% (v/v) Tween. After a 30 min incubation, we quantified the AuNPs by DLS again before centrifuging at 1200 rcf for 30 min at 4 °C and resuspending in PBST (1× PBS, 0.1% (v/v) Tween). The washing by centrifugation process was repeated twice to remove any excess DNA or PEG. We characterized the resulting cleaned AuNP-DNA conjugates using DLS and UV−vis spectrophotometry. We also negatively stained the AuNP-DNA conjugates with 2% (w/v) uranyl acetate solution and collected images using a JEOL 2000FX TEM.

SDS-PAGE and BCA-Based Protein Corona Analysis. It is well-understood that citrate-coated AuNPs can be defined as "quasi-spherical" (i.e., polygonal) while CTAC-coated AuNPs trend more toward "perfectly spherical" by nature of their respective syntheses.[8,61−63] To identify differences in protein identity or relative protein concentration around the surface of citrate-coated or postcitrate-PR CTAC-coated AuNPs, we performed SDS-PAGE and the commercial bicinchoninic acid (BCA) assay analysis according to previous protocols.[43,44,64,65] We prepared stock solutions of 60 nm citrate-coated AuNPs and postcitrate-PR CTAC-coated AuNPs 60 nm. We took aliquots of these stock solutions and modified them with mPEG-SH or HEP as described previously. We prepared AuNPs with two different PEG surface ligand densities, 0.5 or 10 PEG/nm^2, to allow for analysis of protein content on the surface of partially-PEG-saturated and fully-PEG-saturated AuNPs. We thus compared protein content analysis for eight different groups based on two different core nanoparticles (citrate- or CTAC-coated) and four different surface chemistries (citrate, 0.5, 10 PEG/nm^2, and HEP). After surface modification, AuNPs were centrifuged twice to remove excess ligand.

For each of the eight groups, we prepared three 1.5 mL tubes of AuNPs with a volume of 1500 μL and a concentration of 0.49-nM. We targeted a total AuNP surface area of 50 cm^2 for each tube to allow for sufficient protein content for analysis.[43,44] We centrifuged all tubes and removed the supernatant. We diluted the resulting AuNP pellets in 20-μL of nanopure water before pipetting the AuNP solutions into 1000-μL of 100% FBS solution in 1.5 mL LoBind tubes. We incubated the AuNP-protein mixtures for 2 h at 37 °C before washing by centrifugation 3 times to remove excess unbound protein. After each centrifugation, supernatant was removed and the pellet was resuspended in a 1× PBS (dilute from 10×, BioBasic PD8117) 0.05% (v/v) Tween20 solution. After the third wash, we combined pellets from the same group, resuspended to a total volume of 1000-μL using

1× PBS 0.05% (v/v) Tween20 solution, and centrifuged one more time. After removing the supernatant following this centrifugation, we diluted each AuNP pellet using 50-μL of 1× PBS 0.05% (v/v) Tween20, and we measured the AuNP concentration of each group using UV−vis spectrophotometry. We then diluted all pellets to the same nanomolar concentration using 1× PBS 0.05% (v/v) Tween20 solution. To isolate bound protein from the surface of the AuNPs, we added 4-μL of 500-mM dithiothreitol (DTT, Fisher Scientific FERR0861) and 8-μL of NuPAGE 4× LDS sample buffer (ThermoFisher NP0007) to each AuNP solution for every 15-μL of dilute AuNP solution. We then incubated AuNP solutions for 1 h at 70 °C before pelleting the AuNPs by centrifuging at 5000 rcf for 20 min at 4 °C. We recovered the supernatant from each sample to use in our SDS-PAGE and BCA analysis.

For SDS-PAGE analysis, we used 4−12% NuPAGE Bis-Tris precast 1.0 mm protein gels with 12 wells (ThermoFisher NP0322BOX). We mixed 15 μL of the recovered protein supernatant with 6-μL of 4× LDS and 3-μL 500-mM DTT (total final volume of 24-μL). A 2% (v/v) FBS control solution was similarly prepared. We heated the resulting solution to 95 °C for 5 min to denature present protein. We then injected samples into separate wells in the gel. We ran the gel for 55 min at 200 V before transferring the gel to a fixing solution comprised of 10% (v/v) acetic acid (SigmaAldrich 695092) and 40% (v/v) ethanol solution. We let the gel fix for 2 h before rinsing with DI water and staining the gel using 1× SYPRO Tangerine Protein Gel Stain (ThermoFisher S12010). We allowed the stain to act on the gel in a light-protected environment for 1 h. After 1 h, we rinsed the gel with DI water before imaging the gel using an Azure C600 gel imaging system. For image collection, we used an excitation/emission setting compatible with the stain and the ladder PageRuler Plus Prestained 10 250-kDa Protein Ladder used (ThermoFisher PI26619).

Before the BCA analysis of the recovered protein supernatant, we first collected 4 separate 25-μL aliquots of each of the 8 groups (32 total samples) from the original protein supernatant solutions. We added 950-μL of a 10% (w/v) trichloroacetic acid (TCA, SigmaAldrich T9159) in acetone solution to each aliquot and incubated the resulting solutions overnight at −80 °C. We centrifuged the resulting protein precipitates at 18,000 rcf for 15 min at 4 °C, removing the supernatant immediately afterward. We dissolved the newly formed protein pellets using 500-μL of a 0.03% (w/v) sodium deoxycholate (SigmaAldrich, 30970) in water solution, vortexing to ensure complete pellet dissolution. We precipitated the protein again by adding 100-μL of a 72% (w/v) TCA solution in water before incubating the solutions on ice for 30 min. We recovered the protein pellets by centrifuging at 18,000 rcf for 15 min at 4 °C, discarding the supernatant. We dissolved the protein pellets once more in 1000-μL of chilled 100% acetone and incubated at −80 °C for 1 h. We centrifuged protein solutions one more time at 18,000 rcf for 15 min at 4 °C before removing the supernatant and air drying the tubes for ∼10 min.

We added 28-μL of a 2% (w/v) sodium dodecyl sulfate (SDS, Fisher Scientific AC230421000) solution in 1× PBS to each dried protein pellet. We added 10-μL of each sample to separate wells of a 96-well plate. We added 50-μL of serially diluted bovine serum albumin (BSA, SigmaAldrich A7906) to serve as the protein standard curve. We then added 200-μL of working BCA assay solution to all solution-containing wells of the plate before incubating the plate for 1 h at 37 °C. We used a BioTek Synergy Neo2Multi-Mode Plate Reader to measure the 562 nm absorbance of each well, comparing our sample measurements against the BSA concentration serial dilution standard curve measured alongside our samples.

Cell Viability and Cell Uptake. CTAC is innately cytotoxic.[14,15] By removing CTAC and replacing it with citrate using our citrate-PR method, we hypothesized there would be a significant difference in cell viability compared to as-synthesized CTAC-coated AuNPs. To test this, we performed an XTT cell viability assay. We seeded 10,000 cells/well of RAW 264.7 murine macrophages (ATCC TIB-71) into a 96-well plate in 100-μL of complete cell culture media (DMEM high glucose pyruvate, ThermoFisher 11995065) supplemented with 1% (v/v) penicillin-streptomycin (ThermoFisher, 15-140-122) and 10% (v/v) fetal bovine serum (FBS, ThermoFisher 16000044). We let the cells incubate overnight before adding 100-μL of 0.02-nM AuNP solution to each well. For this assay, we used the following AuNP groups: unmodified citrate-coated AuNPs, PEGylated citrate-coated AuNPs (10 PEG/nm^2 target surface density using 5-kDa mPEG-SH), and HEP-conjugated citrate-coated AuNPs (10 HEP/nm^2 target surface density using 13-kDa HEP), as-synthesized CTAC-coated AuNPs, citrate-PR CTAC-coated AuNPs, PEGylated citrate-PR CTAC-coated AuNPs (10 PEG/nm^2 target surface density using 5-kDa mPEG-SH), and HEP-conjugated citrate-PR CTAC-coated AuNPs (10 HEP/nm^2 target surface density using 13-kDa HEP).

For all AuNP formulations, we used 60 nm target diameter AuNPs. We washed all AuNP groups 2 times by centrifugation using 0.1% (v/v) Tween20 solution prior to treating cells to ensure complete removal of any excess unbound molecules. Before adding AuNP doses to cell wells, we incubated the AuNPs in complete cell culture media for 30 min at 37 °C. After incubating cells with AuNP doses for 24 h, we removed the AuNP-containing media and rinsed each well with 1× PBS two times. We used the XTT assay (2,3-Bis(2-Methoxy-4-Nitro-5-Sulfophenyl)-2H-Tetrazolium-5-Carboxanilide, SigmaAldrich 11465015001) method according to the manufacturer's instructions to assess cell viability by measuring the absorbance of formazan in dimethyl sulfoxide (DMSO, SigmaAldrich D2650) at 570 nm using a plate reader. We normalized absorbance values from each AuNP group to the cell-only group after subtracting background absorbance resulting from the well-plate or remaining media.

To collect qualitative images supporting our XTT viability data, we prepared samples for confocal laser scanning microscopy (CLSM) according to prior methods.[47] We used ∼20 mL of a 3:1 v/v mixture of sulfuric acid (H_2SO_4, Avantor 7664-93-9) and hydrogen peroxide (H_2O_2, Sigma-Aldrich 216763) to clean 18 mm glass #1 round microscopy coverslips by immersing the coverslips in the solution for ∼15 min. We rinsed the clean coverslips by thorough rinsing with nanopure water before placing them in a 12-well plate. We treated the 12-well plate with the coverslips using UV light for 10 min before adding 20,000 cells/well in 500-μL of complete cell culture media to each well with a coverslip. We gave the cells 24 h to adhere to the coverslips before adding 150-μL of 0.01-nM AuNP solution. We matched the AuNP groups and media incubation time from our XTT assay analysis, but we did not include as-synthesized CTAC-coated AuNPs as an experimental group, given the lack of measured cell viability (Figure 8A). We incubated the cells with AuNPs for 24 h before the media was removed and washed coverslips three times with 1× PBS. We added 500-μL 4% (w/v) paraformaldehyde (PFA, ThermoFisher AAj19943K2) at room temperature for 10 min to fix cells before staining the cells using the DNA stain, 4′,6-diamidino-2-phenylindole (DAPI, ThermoFisher R37606) and wheat germ agglutinin-CF488A (WGA, Biotium, 29022-1) according to the manufacturer's protocols to label the cell nuclei and cell membrane, respectively. We used a ZEISS LSM 880 inverted confocal laser microscope with a 63× oil immersion objective (1.4 NA) to collect all images. The coverslips were imaged on 35 mm #1.5H glass-bottom dishes. A photomultiplier (PMT) detector, a 405 nm diode laser, a 488 nm argon laser, and a 561 nm diode-pumped solid-state laser were used for fluorescent channels. A main beam splitter (MBS) was used with a 488/561/633 filter. We applied previously detailed light scattering principles of AuNPs to detect nanoparticle presence inside of imaged cells.[46,48]

For additional verification of XTT and CLSM results, we repeated the experiments using 4T1 mammary mouse tumor cells (ATCC CRL-2539). The same seeding densities, treatment groups, dose conditions, and treatment times were used. The primary difference is that for 4T1 cells, RPMI-1640 (ATCC, 30-2001) supplemented with 1% (v/v) penicillin-streptomycin and 10% (v/v) FBS was used for culturing and seeding cells.

■ ASSOCIATED CONTENT

Supporting Information

The Supporting Information is available free of charge at https://pubs.acs.org/doi/10.1021/acsanm.4c04838.

Equations, tables, and figures supporting the main manuscript; spreadsheet resource for researcher use in AuNP synthesis (PDF)

Target diameter gold nanoparticle growth calculator (XLSX)

■ AUTHOR INFORMATION

Corresponding Author

Stefan Wilhelm − *Stephenson School of Biomedical Engineering and Institute for Biomedical Engineering, Science, and Technology (IBEST), University of Oklahoma, Norman, Oklahoma 73019, United States; Stephenson Cancer Center, University of Oklahoma Health Sciences Center, Oklahoma City, Oklahoma 73104, United States;* orcid.org/0000-0003-2167-6221; Email: stefan.wilhelm@ou.edu

Authors

Alex N. Frickenstein − *Stephenson School of Biomedical Engineering, University of Oklahoma, Norman, Oklahoma 73019, United States*

Nathan Means − *Stephenson School of Biomedical Engineering, University of Oklahoma, Norman, Oklahoma 73019, United States*

Yuxin He − *Stephenson School of Biomedical Engineering, University of Oklahoma, Norman, Oklahoma 73019, United States*

Luke Whitehead − *Stephenson School of Biomedical Engineering, University of Oklahoma, Norman, Oklahoma 73019, United States*

Tekena Harcourt − *Stephenson School of Biomedical Engineering, University of Oklahoma, Norman, Oklahoma 73019, United States*

Zain Malik − *Stephenson School of Biomedical Engineering, University of Oklahoma, Norman, Oklahoma 73019, United States*

Vinit Sheth − *Stephenson School of Biomedical Engineering, University of Oklahoma, Norman, Oklahoma 73019, United States*

Logan Longacre − *Stephenson School of Biomedical Engineering, University of Oklahoma, Norman, Oklahoma 73019, United States*

Haley Taffe − *Stephenson School of Biomedical Engineering, University of Oklahoma, Norman, Oklahoma 73019, United States*

Lin Wang − *Stephenson School of Biomedical Engineering, University of Oklahoma, Norman, Oklahoma 73019, United States;* orcid.org/0000-0003-4636-8225

Isabella McSpadden − *Stephenson School of Biomedical Engineering, University of Oklahoma, Norman, Oklahoma 73019, United States*

Connor Baroody − *Stephenson School of Biomedical Engineering, University of Oklahoma, Norman, Oklahoma 73019, United States*

Wen Yang − *Stephenson School of Biomedical Engineering, University of Oklahoma, Norman, Oklahoma 73019, United States;* orcid.org/0000-0001-9206-0868

Yan D. Zhao − *Department of Biostatistics and Epidemiology, University of Oklahoma Health Sciences Center, Oklahoma City, Oklahoma 73012, United States; Stephenson Cancer Center, University of Oklahoma Health Sciences Center, Oklahoma City, Oklahoma 73104, United States*

Complete contact information is available at: https://pubs.acs.org/10.1021/acsanm.4c04838

Funding

This work was supported in part by awards from NIH COBRE (P20GM135009), NIH MIRA R35 (1R35GM150758), NSF CAREER (2048130), OCAST (HR20-106), and the University of Oklahoma Office Vice President for Research and Partnerships (OVPRP) Postdoc Match Program and Strategic Equipment Investment Program (SEIP).

Notes

The authors declare no competing financial interest.

■ ACKNOWLEDGMENTS

Special thanks to Dr. Paul DeAngelis and Dixy Green for providing the activated heparosan (HEP) used in this study (funded in part by the Presbyterian Research Foundation, Team Science Grant). Thanks also to Dr. Steven Foster and the Mass Spectrometry, Proteomics, and Metabolomics (MSPM) Core for assistance in ICP-MS data collection. The authors would like to thank Dr. Preston Larson and Dr. Julian Sabisch from the OU SRNML for their assistance in collecting TEM and SEM images used in this study. The authors also acknowledge Dr. Ben Fowler and the Oklahoma Medical Research Foundation (OMRF) for support in confocal microscopy. The authors thank Dr. Nathan Donahue for his support in developing methods and providing insight for SP-ICP-MS data collection. The authors acknowledge Dr. Tahrima Rouf, Dr. John Clegg, and Serana Nelson for their help collecting FTIR spectroscopy results. The authors additionally thank members of the Chen Lab at OU for their support in completing SDS-PAGE experiments. Special thanks to the Chan Lab at UofT for providing molar extinction coefficient data and equations used in predictive nanoparticle synthesis. Finally, the authors thank Sarah Butterfield, Abbie Thomas, Hamilton Young, Tyler Wilson, and Shanxin Lyu for their assistance with experiments. Parts of this work were originally presented as chapters in Dr. Alex Frickenstein's thesis "Improving Quantification of Nanoscale Interactions by Engineering Monodisperse Gold Nanoparticles".[66]

■ REFERENCES

(1) Arnida; Janát-Amsbury, M. M.; Ray, A.; Peterson, C. M.; Ghandehari, H. Geometry and surface characteristics of gold nanoparticles influence their biodistribution and uptake by macrophages. *Eur. J. Pharm. Biopharm.* **2011**, *77* (3), 417−423.

(2) Bai, X.; Wang, Y.; Song, Z.; Feng, Y.; Chen, Y.; Zhang, D.; Feng, L. The basic properties of gold nanoparticles and their applications in tumor diagnosis and treatment. *International Journal of Molecular Sciences* **2020**, *21* (7), 2480.

(3) Yeh, Y.-C.; Creran, B.; Rotello, V. M. Gold nanoparticles: preparation, properties, and applications in bionanotechnology. *Nanoscale* **2012**, *4* (6), 1871−1880.

(4) Zhang, Y.; Elechalawar, C. K.; Yang, W.; Frickenstein, A. N.; Asfa, S.; Fung, K.-M.; Murphy, B. N.; Dwivedi, S. K.; Rao, G.; Dey, A.; Wilhelm, S.; Bhattacharya, R.; Mukherjee, P. Disabling partners in crime: Gold nanoparticles disrupt multicellular communications within the tumor microenvironment to inhibit ovarian tumor aggressiveness. *Mater. Today* **2022**, *56*, 79−95.

(5) Sindhwani, S.; Syed, A. M.; Ngai, J.; Kingston, B. R.; Maiorino, L.; Rothschild, J.; MacMillan, P.; Zhang, Y.; Rajesh, N. U.; Hoang, T.;

Wu, J. L. Y.; Wilhelm, S.; Zilman, A.; Gadde, S.; Sulaiman, A.; Ouyang, B.; Lin, Z.; Wang, L.; Egeblad, M.; Chan, W. C. W. The entry of nanoparticles into solid tumours. *Nat. Mater.* **2020**, *19* (5), 566−575.

(6) Poon, W.; Zhang, Y.-N.; Ouyang, B.; Kingston, B. R.; Wu, J. L. Y.; Wilhelm, S.; Chan, W. C. W. Elimination Pathways of Nanoparticles. *ACS Nano* **2019**, *13* (5), 5785−5798.

(7) Wang, L.; Quine, S.; Frickenstein, A. N.; Lee, M.; Yang, W.; Sheth, V. M.; Bourlon, M. D.; He, Y.; Lyu, S.; Garcia-Contreras, L.; Zhao, Y. D.; Wilhelm, S. Exploring and Analyzing the Systemic Delivery Barriers for Nanoparticles. *Adv. Funct. Mater.* **2024**, *34* (8), No. 2308446.

(8) Perrault, S. D.; Chan, W. C. W. Synthesis and Surface Modification of Highly Monodispersed, Spherical Gold Nanoparticles of 50−200 nm. *J. Am. Chem. Soc.* **2009**, *131* (47), 17042−17043.

(9) Kus-Liśkiewicz, M. A.-O.; Fickers, P. A.-O.; Ben Tahar, I. Biocompatibility and Cytotoxicity of Gold Nanoparticles: Recent Advances in Methodologies and Regulations. *Int. J. Mol. Sci.* **2021**, *22* (20), 10952.

(10) Kang, M. S.; Lee, S. Y.; Kim, K. S.; Han, D.-W. State of the Art Biocompatible Gold Nanoparticles for Cancer Theragnosis Pharmaceutics [Online], 2020.

(11) Elechalawar, C. K.; Rao, G.; Gulla, S. K.; Patel, M. M.; Frickenstein, A.; Means, N.; Roy, R. V.; Tsiokas, L.; Asfa, S.; Panja, P.; Rao, C.; Wilhelm, S.; Bhattacharya, R.; Mukherjee, P. Gold Nanoparticles Inhibit Macropinocytosis by Decreasing KRAS Activation. *ACS Nano* **2023**, *17* (10), 9326−9337.

(12) Frickenstein, A. N.; Mukherjee, S.; Harcourt, T.; He, Y.; Sheth, V.; Wang, L.; Malik, Z.; Wilhelm, S. Quantification of monodisperse and biocompatible gold nanoparticles by single-particle ICP-MS. *Anal Bioanal Chem.* **2023**, *415*, 4353−4366.

(13) Xu, M.; Soliman, M. G.; Sun, X.; Pelaz, B.; Feliu, N.; Parak, W. J.; Liu, S. How Entanglement of Different Physicochemical Properties Complicates the Prediction of in Vitro and in Vivo Interactions of Gold Nanoparticles. *ACS Nano* **2018**, *12* (10), 10104−10113.

(14) Liu, N.; Zhang, H.; Zhao, J.; Xu, Y.; Ge, F. Mechanisms of cetyltrimethyl ammonium chloride-induced toxicity to photosystem II oxygen evolution complex of Chlorella vulgaris F1068. *J. Hazard. Mater.* **2020**, *383*, No. 121063.

(15) Tang, M.; Zhang, P.; Liu, J.; Long, Y.; Cheng, Y.; Zheng, H. Cetyltrimethylammonium chloride-loaded mesoporous silica nanoparticles as a mitochondrion-targeting agent for tumor therapy. *RSC Adv.* **2020**, *10* (29), 17050−17057.

(16) Chen, B.-M.; Cheng, T.-L.; Roffler, S. R. Polyethylene Glycol Immunogenicity: Theoretical, Clinical, and Practical Aspects of Anti-Polyethylene Glycol Antibodies. *ACS Nano* **2021**, *15* (9), 14022−14048.

(17) Ju, Y.; Lee, W. S.; Pilkington, E. H.; Kelly, H. G.; Li, S.; Selva, K. J.; Wragg, K. M.; Subbarao, K.; Nguyen, T. H. O.; Rowntree, L. C.; Allen, L. F.; Bond, K.; Williamson, D. A.; Truong, N. P.; Plebanski, M.; Kedzierska, K.; Mahanty, S.; Chung, A. W.; Caruso, F.; Wheatley, A. K.; Juno, J. A.; Kent, S. J. Anti-PEG Antibodies Boosted in Humans by SARS-CoV-2 Lipid Nanoparticle mRNA Vaccine. *ACS Nano* **2022**, *16* (8), 11769−11780.

(18) Donahue, N. D.; Sheth, V.; Frickenstein, A. N.; Holden, A.; Kanapilly, S.; Stephan, C.; Wilhelm, S. Absolute Quantification of Nanoparticle Interactions with Individual Human B Cells by Single Cell Mass Spectrometry. *Nano Lett.* **2022**, *22* (10), 4192−4199.

(19) Donahue, N. D.; Francek, E. R.; Kiyotake, E.; Thomas, E. E.; Yang, W.; Wang, L.; Detamore, M. S.; Wilhelm, S. Assessing nanoparticle colloidal stability with single-particle inductively coupled plasma mass spectrometry (SP-ICP-MS). *Anal. Bioanal. Chem.* **2020**, *412* (22), 5205−5216.

(20) Donahue, N. D.; Kanapilly, S.; Stephan, C.; Marlin, M. C.; Francek, E. R.; Haddad, M.; Guthridge, J.; Wilhelm, S. Quantifying Chemical Composition and Reaction Kinetics of Individual Colloidally Dispersed Nanoparticles. *Nano Lett.* **2022**, *22* (1), 294−301.

(21) Wilhelm, S.; Bensen, R.; Kothapalli, R.; Burgett, A.; Merrifield, R.; Stephan, C. *Quantification of Gold Nanoparticle Uptake into Cancer Cells using Single Cell ICP-MS*; PerkinElmer Appl Note, 2018.

(22) Lee, J. C.; Donahue, N. D.; Mao, A. S.; Karim, A.; Komarneni, M.; Thomas, E. E.; Francek, E. R.; Yang, W.; Wilhelm, S. Exploring Maleimide-Based Nanoparticle Surface Engineering to Control Cellular Interactions. *ACS Applied Nano Materials* **2020**, *3* (3), 2421−2429.

(23) Zheng, Y.; Ma, Y.; Zeng, J.; Zhong, X.; Jin, M.; Li, Z.-Y.; Xia, Y. Seed-Mediated Synthesis of Single-Crystal Gold Nanospheres with Controlled Diameters in the Range 5−30 nm and their Self-Assembly upon Dilution. *Chem. - Asian J.* **2013**, *8* (4), 792−799.

(24) Zheng, Y.; Zhong, X.; Li, Z.; Xia, Y. Successive, Seed-Mediated Growth for the Synthesis of Single-Crystal Gold Nanospheres with Uniform Diameters Controlled in the Range of 5−150 nm. *Part. Part. Syst. Charact.* **2014**, *31* (2), 266−273.

(25) Schulz, F.; Pavelka, O.; Lehmkühler, F.; Westermeier, F.; Okamura, Y.; Mueller, N. S.; Reich, S.; Lange, H. Structural order in plasmonic superlattices. *Nat. Commun.* **2020**, *11* (1), 3821.

(26) Li, J.; Zhu, B.; Zhu, Z.; Zhang, Y.; Yao, X.; Tu, S.; Liu, R.; Jia, S.; Yang, C. J. Simple and Rapid Functionalization of Gold Nanorods with Oligonucleotides Using an mPEG-SH/Tween 20-Assisted Approach. *Langmuir* **2015**, *31* (28), 7869−7876.

(27) Khlebtsov, N. G. Determination of Size and Concentration of Gold Nanoparticles from Extinction Spectra. *Anal. Chem.* **2008**, *80* (17), 6620−6625.

(28) Shafiqa, A. R.; Abdul Aziz, A.; Mehrdel, B. Nanoparticle Optical Properties: Size Dependence of a Single Gold Spherical Nanoparticle. *J. Phys.: Conf. Ser.* **2018**, *1083* (1), No. 012040.

(29) Khoury, R. A.; Ranasinghe, J. C.; Dikkumbura, A. S.; Hamal, P.; Kumal, R. R.; Karam, T. E.; Smith, H. T.; Haber, L. H. Monitoring the Seed-Mediated Growth of Gold Nanoparticles Using in Situ Second Harmonic Generation and Extinction Spectroscopy. *J. Phys. Chem. C* **2018**, *122* (42), 24400−24406.

(30) Bastús, N. G.; Comenge, J.; Puntes, V. Kinetically Controlled Seeded Growth Synthesis of Citrate-Stabilized Gold Nanoparticles of up to 200 nm: Size Focusing versus Ostwald Ripening. *Langmuir* **2011**, *27* (17), 11098−11105.

(31) Haddad, M.; Frickenstein, A. N.; Wilhelm, S. High-throughput single-cell analysis of nanoparticle-cell interactions. *TrAC Trends in Analytical Chemistry* **2023**, *166*, No. 117172.

(32) Maguire, C. A.-O.; Rösslein, M.; Wick, P.; Prina-Mello, A. A.-O. Characterisation of particles in solution − a perspective on light scattering and comparative technologies. *Sci. Technol. Adv. Mater.* **2018**, *19* (1), 732−745.

(33) Balog, S. Hydrodynamic Radius of Polymer-Coated Nanoparticles Measured by Taylor Dispersion: A Mathematical Model. *Anal. Chem.* **2020**, *92* (15), 10693−10699.

(34) Lee, S.; Bi, X.; Reed, R. B.; Ranville, J. F.; Herckes, P.; Westerhoff, P. Nanoparticle Size Detection Limits by Single Particle ICP-MS for 40 Elements. *Environ. Sci. Technol.* **2014**, *48* (17), 10291−10300.

(35) Giorgi, F.; Curran, J. M.; Gilliland, D.; La Spina, R.; Whelan, M.; Patterson, E. A. Limitations of Nanoparticles Size Characterization by Asymmetric Flow Field-Fractionation Coupled with Online Dynamic Light Scattering. *Chromatographia* **2021**, *84* (2), 199−206.

(36) Chauhan, M. K.; Sachdeva, A.; Ansari, L.; Gugulothu, D., Manufacturing Process of Nanoparticles. In *Pharmaceutical Process Engineering and Scale-up Principles*, Jindal, A. B., Ed.; Springer Nature Switzerland: Cham, 2023; pp 151−172.

(37) Tran, M.; DePenning, R.; Turner, M.; Padalkar, S. Effect of citrate ratio and temperature on gold nanoparticle size and morphology. *Materials Research Express* **2016**, *3* (10), No. 105027.

(38) Yazdani, S.; Daneshkhah, A.; Diwate, A.; Patel, H.; Smith, J.; Reul, O.; Cheng, R.; Izadian, A.; Hajrasouliha, A. R. Model for Gold Nanoparticle Synthesis: Effect of pH and Reaction Time. *ACS Omega* **2021**, *6* (26), 16847−16853.

(39) Yoon, S.; Kim, C.; Lee, B.; Lee, J. H. From a precursor to an etchant: spontaneous inversion of the role of Au(iii) chloride for one-

pot synthesis of smooth and spherical gold nanoparticles. *Nanoscale Advances* **2019**, *1* (6), 2157−2161.

(40) Farkas, N.; Kramar, J. A. Dynamic light scattering distributions by any means. *J. Nanopart. Res.* **2021**, *23* (5), 120.

(41) Stetefeld, J.; McKenna, S. A.; Patel, T. R. Dynamic light scattering: a practical guide and applications in biomedical sciences. *Biophysical Reviews* **2016**, *8* (4), 409−427.

(42) Deangelis, P. L. Heparosan, a promising 'naturally good' polymeric conjugating vehicle for delivery of injectable therapeutics. *Expert Opinion on Drug Delivery* **2015**, *12* (3), 349−352.

(43) Yang, W.; Frickenstein, A. N.; Sheth, V.; Holden, A.; Mettenbrink, E. M.; Wang, L.; Woodward, A. A.; Joo, B. S.; Butterfield, S. K.; Donahue, N. D.; Green, D. E.; Thomas, A. G.; Harcourt, T.; Young, H.; Tang, M.; Malik, Z. A.; Harrison, R. G.; Mukherjee, P.; DeAngelis, P. L.; Wilhelm, S. Controlling Nanoparticle Uptake in Innate Immune Cells with Heparosan Polysaccharides. *Nano Lett.* **2022**, *22* (17), 7119−7128.

(44) Yang, W.; Wang, L.; Fang, M.; Sheth, V.; Zhang, Y.; Holden, A. M.; Donahue, N. D.; Green, D. E.; Frickenstein, A. N.; Mettenbrink, E. M.; Schwemley, T. A.; Francek, E. R.; Haddad, M.; Hossen, M. N.; Mukherjee, S.; Wu, S.; DeAngelis, P. L.; Wilhelm, S. Nanoparticle Surface Engineering with Heparosan Polysaccharide Reduces Serum Protein Adsorption and Enhances Cellular Uptake. *Nano Lett.* **2022**, *22* (5), 2103−2111.

(45) Perera, Y. R.; Xu, J. X.; Amarasekara, D. L.; Hughes, A. C.; Abbood, I.; Fitzkee, N. C. *Understanding the Adsorption of Peptides and Proteins onto PEGylated Gold Nanoparticles Molecules [Online]*, 2021.

(46) Syed, A. M.; Sindhwani, S.; Wilhelm, S.; Kingston, B. R.; Lee, D. S. W.; Gommerman, J. L.; Chan, W. C. W. Three-Dimensional Imaging of Transparent Tissues via Metal Nanoparticle Labeling. *J. Am. Chem. Soc.* **2017**, *139* (29), 9961−9971.

(47) Sheth, V.; Chen, X.; Mettenbrink, E. M.; Yang, W.; Jones, M. A.; M'Saad, O.; Thomas, A. G.; Newport, R. S.; Francek, E.; Wang, L.; Frickenstein, A. N.; Donahue, N. D.; Holden, A.; Mjema, N. F.; Green, D. E.; DeAngelis, P. L.; Bewersdorf, J.; Wilhelm, S. Quantifying Intracellular Nanoparticle Distributions with Three-Dimensional Super-Resolution Microscopy. *ACS Nano* **2023**, *17* (9), 8376−8392.

(48) Wang, F.; Chen, B.; Yan, B.; Yin, Y.; Hu, L.; Liang, Y.; Song, M.; Jiang, G. *Scattered Light Imaging Enables Real-Time Monitoring of Label-Free Nanoparticles and Fluorescent Biomolecules in Live Cells.* **2019**, *141* (36), 14043−14047.

(49) Hua, T.; Zhang, X.; Tang, B.; Chang, C.; Liu, G.; Feng, L.; Yu, Y.; Zhang, D.; Hou, J. Tween-20 transiently changes the surface morphology of PK-15 cells and improves PCV2 infection. *BMC Vet. Res.* **2018**, *14* (1), 138.

(50) Turkevich, J.; Stevenson, P. C.; Hillier, J. A study of the nucleation and growth processes in the synthesis of colloidal gold. *Discuss. Faraday Soc.* **1951**, *11* (0), 55−75.

(51) Kumar, V.; Sharma, N.; Maitra, S. S. In vitro and in vivo toxicity assessment of nanoparticles. *International Nano Letters* **2017**, *7* (4), 243−256.

(52) Hoshyar, N.; Gray, S.; Han, H.; Bao, G. The effect of nanoparticle size on in vivo pharmacokinetics and cellular interaction. *Nanomedicine* **2016**, *11* (6), 1748−6963.

(53) Mitchell, M. J.; Billingsley, M. M.; Haley, R. M.; Wechsler, M. E.; Peppas, N. A.; Langer, R. Engineering precision nanoparticles for drug delivery. *Nat. Rev. Drug Discovery* **2021**, *20* (2), 101−124.

(54) Chemnitzer, R. Strategies for Achieving the Lowest Possible Detection Limits in ICP-MS. *Spectroscopy* **2019**, *34* (10), 12−16.

(55) Anastassopoulou, J. D., Mass and FT-IR Spectra of Quaternary Ammonium Surfactants. In *Chemistry and Properties of Biomolecular Systems*; Rizzarelli, E.; Theophanides, T., Eds.; Springer Netherlands: Dordrecht, 1991; pp 1−9.

(56) Gurunathan, S.; Han, J.; Park, J. H.; Kim, J.-H. A green chemistry approach for synthesizing biocompatible gold nanoparticles. *Nanoscale Res. Lett.* **2014**, *9* (1), 248.

(57) Kurrey, R.; Deb, M. K.; Shrivas, K.; Khalkho, B. R.; Nirmalkar, J.; Sinha, D.; Jha, S. Citrate-capped gold nanoparticles as a sensing probe for determination of cetyltrimethylammonium surfactant using FTIR spectroscopy and colorimetry. *Anal. Bioanal. Chem.* **2019**, *411* (26), 6943−6957.

(58) Villarreal, E.; Li, G. G.; Zhang, Q.; Fu, X.; Wang, H. Nanoscale Surface Curvature Effects on Ligand−Nanoparticle Interactions: A Plasmon-Enhanced Spectroscopic Study of Thiolated Ligand Adsorption, Desorption, and Exchange on Gold Nanoparticles. *Nano Lett.* **2017**, *17* (7), 4443−4452.

(59) Chou, L. Y. T.; Zagorovsky, K.; Chan, W. C. W. DNA assembly of nanoparticle superstructures for controlled biological delivery and elimination. *Nat. Nanotechnol.* **2014**, *9* (2), 148−155.

(60) Zhang, Z.-L.; Pang, D.-W.; Yuan, H.; Cai, R.-X.; Abruña, H. D. Electrochemical DNA sensing based on gold nanoparticle amplification. *Anal. Bioanal. Chem.* **2005**, *381* (4), 833−838.

(61) Yang, T.-H.; Shi, Y.; Janssen, A.; Xia, Y. Surface Capping Agents and Their Roles in Shape-Controlled Synthesis of Colloidal Metal Nanocrystals. *Angew. Chem., Int. Ed.* **2020**, *59* (36), 15378−15401.

(62) Scarabelli, L.; Sánchez-Iglesias, A.; Pérez-Juste, J.; Liz-Marzán, L. M. A "Tips and Tricks" Practical Guide to the Synthesis of Gold Nanorods. *J. Phys. Chem. Lett.* **2015**, *6* (21), 4270−4279.

(63) Personick, M. L.; Mirkin, C. A. Making Sense of the Mayhem behind Shape Control in the Synthesis of Gold Nanoparticles. *J. Am. Chem. Soc.* **2013**, *135* (49), 18238−18247.

(64) Walkey, C. D.; Olsen, J. B.; Song, F.; Liu, R.; Guo, H.; Olsen, D. W. H.; Cohen, Y.; Emili, A.; Chan, W. C. W. Protein Corona Fingerprinting Predicts the Cellular Interaction of Gold and Silver Nanoparticles. *ACS Nano* **2014**, *8* (3), 2439−2455.

(65) Walkey, C. D.; Olsen, J. B.; Guo, H.; Emili, A.; Chan, W. C. W. Nanoparticle Size and Surface Chemistry Determine Serum Protein Adsorption and Macrophage Uptake. *J. Am. Chem. Soc.* **2012**, *134* (4), 2139−2147.

(66) Frickenstein, A. N. Improving Quantification of Nanoscale Interactions by Engineering Monodisperse Gold Nanoparticles; Doctoral Dissertation; University of Oklahoma, ShareOK, 2023.